Available online at www.sciencedirect.com

ScienceDirect

Geochimica et Cosmochimica Acta 300 (2021) 192–214

Geochimica et Cosmochimica Acta

www.elsevier.com/locate/gca

# Antigorite dehydration fluids boost carbonate mobilisation and crustal $CO_2$ outgassing in collisional orogens

Lisa Eberhard *, Thomas Pettke

*Institute of Geological Sciences, University of Bern, Baltzerstrasse 1+3, CH-3012 Bern, Switzerland*

Received 24 September 2020; accepted in revised form 17 February 2021; available online 1 March 2021

**Abstract**

The processes of carbon mobilisation at convergent plate boundaries are hotly debated. Recent findings suggest that carbon release along subduction geothermal gradients may well be more relevant than previously thought; however, it has remained difficult to achieve steady state atmospheric $CO_2$ conditions over geological time scales based on current volatile cycle models. Here, we report on meta-ophicarbonate rocks in the contact metamorphic aureole of the Bergell intrusion, Val Malenco, European Alps, that reached T-P conditions of at least 650 °C at 0.35 GPa. We demonstrate by combined field evidence, geochemistry, and closed-system thermodynamic modelling that over 50% of the rock carbonate has been mobilised locally in response to reactive fluid flow upon progressive isobaric heating from 350 to >650 °C. Despite complete mineral transformation at the antigorite + calcite devolatilisation reaction, the resulting tremolite-ophicarbonate preserves the original ophicarbonate texture by olivine-chlorite clasts, representing the former antigorite-serpentinite fraction, embedded in a monomineralic tremolite matrix formed from the calcite fraction that often exceeded 50 vol%. Closed system thermodynamic modelling based on an ophicarbonate composition of 80 wt% serpentinite +20 wt% calcite reveals that rock-buffered fluid $X_{CO2}$ values evolve from <0.09 to as high as ~0.16, and the total $H_2O$-$CO_2$ fluid fraction released may be as high as 14 wt%; values that are highly sensitive to bulk ophicarbonate composition.

Major to trace element geochemistry reveals a history of peridotite melt depletion followed by ocean floor hydration and ophicarbonate formation, consistent with the ocean continent transition (OCT) setting of the mantle rocks in the Mesozoic. This is demonstrated by positive anomalies in B, U, As, Sb, Bi, and W, and by bulk rock and notably carbonate primitive mantle normalised REE patterns that are basically identical to that of calcite precipitated from Jurassic seawater except for its negative Eu anomaly. Prograde metamorphic tremolite and diopside possess enrichments notably in Sr and REE inherited from reactant calcite, as is also supported by a good match between measured and modelled silicate mineral compositions. Specific geochemical characteristics of the prograde meta-ophicarbonate rocks imply fluid mediated, open system processes. Antigorite dehydration fluid ingress, likely produced in neighbouring antigorite-serpentinites, may have shifted bulk tremolite ophicarbonate rock compositions towards higher $SiO_2$/MgO ratios along with an increase in B contents and depletion in fluid mobile elements such as As, Sb, and Sr.

The massive, contact metamorphic $CO_2$ mobilisation documented here occurred at P-T conditions that are similar to those that can be achieved in collisional orogenic settings, whose clockwise P-T-t paths are often characterised by further heating upon initial decompression. They thus evolve at large angle to devolatilisation reactions and silicate-carbonate rock-buffered fluid $X_{CO2}$ isopleths, thus fostering carbon mobilisation towards metamorphic peak temperatures at moderate to low pressures (in the region of between >700 °C – 1.0 GPa and >600 °C – 0.3 GPa). Barrovian metamorphism, too, can reach T-P conditions of 800 °C – 1 GPa. Amagmatic $CO_2$ mobilised this way will eventually reach the atmosphere via dispersion in the groundwater

* Corresponding author at: Bayerisches Geoinstitut, University of Bayreuth, Universitätsstrasse 30, D-95440 Bayreuth, Germany.
*E-mail addresses:* lisa1.eberhard@uni-bayreuth.de (L. Eberhard), pettke@geo.unibe.ch (T. Pettke).

https://doi.org/10.1016/j.gca.2021.02.030

table and diffuse outgassing. Despite the huge uncertainties associated with quantification of such metamorphic carbon fluxes, geological time scale global carbon cycling models should more rigorously explore the significance of these contributions.


*Keywords:* Ophicarbonate; $CO_2$ outgassing; Contact metamorphism; Amagmatic $CO_2$

## 1. INTRODUCTION

Convergent plate boundaries arguably play a major role in the global carbon cycle over geological time scales; however, relevant carbonate recycling processes and fluxes continue to be hotly debated. Among these, estimates for modern subduction zone carbon cycling back to the convecting mantle range between 80% and "very little" (e.g., Gorman et al., 2006; Dasgupta and Hirschmann, 2010; Dasgupta, 2013; Kelemen and Manning, 2015), and estimates for the fraction of total subducted carbon returned to the atmosphere also vary widely. These studies mostly agree that subducted carbon significantly outweighs convergent plate volcanic $CO_2$ output. Moreover, estimates of $CO_2$ masses transferred via volcanic degassing to the atmosphere (e.g., Gorman et al., 2006) are lower than estimates for atmospheric $CO_2$ fixation via silicate weathering (e.g., Berner, 2004), calling for additional $CO_2$ emission from the lithosphere-asthenosphere if steady state conditions were to be achieved over millions of years. Major events of magmatism not associated with convergent margins such as flood basalt eruptions can generate catastrophic $CO_2$ emissions (e.g., Ganino and Arndt, 2009); however, they cannot effectively compensate for the above imbalance. General agreement has emerged that most $CO_2$ from subducting slabs is lost in forearc regions (e.g, Kerrick and Connolly, 2001; Gorman et al., 2006). However, part of it may re-precipitate as metasomatic carbonate-bearing rocks when fluids migrate through different lithologies along the slab interface (Piccoli et al., 2016; Scambelluri et al., 2016) or can be fixed in the cold mantle wedge nose (e.g., Sieber et al., 2018; Albers et al., 2019). Nevertheless, forearc $CO_2$ seeps into the hydrosphere (e.g., Kerrick, 2001; Campbell et al., 2002) and represents a yet poorly constrained, continuous, amagmatic $CO_2$ supply to the atmosphere.

Carbon flux estimates with progressive metamorphism strongly depend on bulk rock compositions, the thermal regime, and closed system versus open system thermodynamic considerations, with or without mineral dissolution. Besides volcanic outgassing, significant fluid-mediated mobility of carbon in subduction zones has recently been suggested for natural examples documenting carbonate dissolution and metasomatic carbonate precipitation (e.g., Ague and Nicolescu, 2014; Piccoli et al., 2016; Scambelluri et al., 2016; Vitale-Brovarone et al., 2018). Carbon mobility in the subduction environment, that is at high pressures combined with moderate temperatures, critically depends on mineral solubilities in aqueous fluids migrating across different lithologies of the subduction plate interface (Gorman et al., 2006; Ague and Nicolescu, 2014; Kelemen and Manning, 2015; Menzel et al., 2019, 2020), and carbon solubility in aqueous fluids can significantly be enhanced when they contain dissolved silicate (e.g., Tumiati et al., 2017).

Non-volcanic carbon emissions to the atmosphere have remained poorly constrained to date. Crustal carbon has been identified as a prominent source of volcanic degassing along continental arcs (Mason et al., 2017). While assimilation of crustal carbonate can be significant in calcalkaline magmas (e.g., Spandler et al., 2012), $CO_2$ release upon contact metamorphism around magma reservoirs may be much more relevant for crustal carbon mobilisation (e.g., Spear, 1993; Kerrick and Caldeira, 1998; Svensen and Jamtveit, 2010); yet, how relevant such contributions are has remained unclear. Contact metamorphism around calcalkaline magma reservoirs takes place at high temperatures and moderate to low pressures where $CO_2$ mobilisation is maximised (e.g., Trommsdorff and Evans, 1977; Kerrick and Caldeira, 1998). To a first order, similar high temperature – moderate pressure conditions can also be attained during regional metamorphism. Apart from a few recent contributions (e.g., Becker et al., 2008; Evans et al., 2008; Svensen and Jamtveit, 2010; Evans, 2011; Groppo et al., 2013, 2017, 2020; Rapa et al., 2017), processes of regional metamorphic $CO_2$ degassing from orogenic belts have remained little explored, however.

Here we present the late Alpine, prograde contact metamorphic evolution of an ophicarbonate horizon formed at the Tethyan ocean floor. Ophicarbonates are an ideal rock to investigate open-system, rock-buffered carbonate mobilisation because of their characteristic textures and comparatively simple petrology and composition. Our field-based results document massive carbonate mobilisation along migration pathways of aqueous fluids liberated from antigorite dehydration at low pressure and high temperatures. We demonstrate that carbon mobility is much more effective in open systems at moderate to low-P amphibolite facies conditions than at HP subduction conditions. We then discuss the potential of contact metamorphism and metamorphism in collisional orogens for amagmatic carbon mobilisation. We conclude that metamorphic carbon outgassing can be highly relevant and offers an important background $CO_2$ supply to the atmosphere (e.g., Kerrick and Caldeira, 1998; Becker et al., 2008; Evans et al., 2008; Svensen and Jamtveit, 2010; Groppo et al., 2017; Stewart et al., 2019) over millions of years, yet to be better constrained and more widely incorporated into global carbon flux models over geological timescales.

## 2. GEOLOGICAL FRAMEWORK OF VAL MALENCO META-OPHICARBONATES

The Val Malenco ultramafic unit in N Italy, European Alps, hosts an oceanic ophicarbonate series (Trommsdorff

and Evans, 1977) embedded in antigorite-serpentinite striking perpendicular to the Bergell intrusion, which was emplaced under retrograde Alpine regional metamorphic conditions in the early Oligocene (Fig. 1a, b; Trommsdorff and Evans, 1977; Trommsdorff and Connolly, 1996; Pozzorini and Früh-Green, 1996). This unit represents a member of the rifted margin of the Adriatic continent (Trommsdorff et al., 1993; Müntener and Hermann, 1996) composed of variably melt-depleted and refertilised former subcontinental lithospheric mantle (Müntener et al., 2004, 2010) exposed to the Jurassic Piemont Ligurian ocean floor, forming serpentinites and ophicarbonate, capped in part by platform carbonates. Consequently, the Val Malenco unit is interpreted as a classical ocean-continent-transition (OCT) sequence (see Trommsdorff et al., 2005, and references therein for an excellent illustration). During the Alpine orogeny these rocks were subducted to moderate depths and attained peak Alpine metamorphic conditions of ~450 °C/0.6–0.7 GPa (Guntli and Liniger, 1989).

During early Alpine exhumation, an up to 1.5 km thick contact aureole developed in response to the composite Bergell intrusion at ~32 Ma (Trommsdorff and Evans, 1972; Trommsdorff and Connolly, 1996; Clément et al., 2019). Meta-ophicarbonates strike approximately perpendicular to the contact metamorphic isograds and cover conditions of ~350 to >650 °C (this work) at ~0.35 GPa (Trommsdorff and Connolly, 1996). The two to a few hundred metre thick meta-ophicarbonate series is mostly embedded in hydrous mantle rocks except for locality d where ophicarbonate is in tectonic contact with the lower Austroalpine Margna basement gneisses (Fig. 1a).

## 3. ANALYTICAL METHODS

Sample mineralogy was determined by optical polarisation microscopy, aided by RAMAN spectroscopy. Half of each slide was coloured for carbonates employing an in-house etching-staining procedure allowing for selective colouring of different carbonate types: Calcite turns

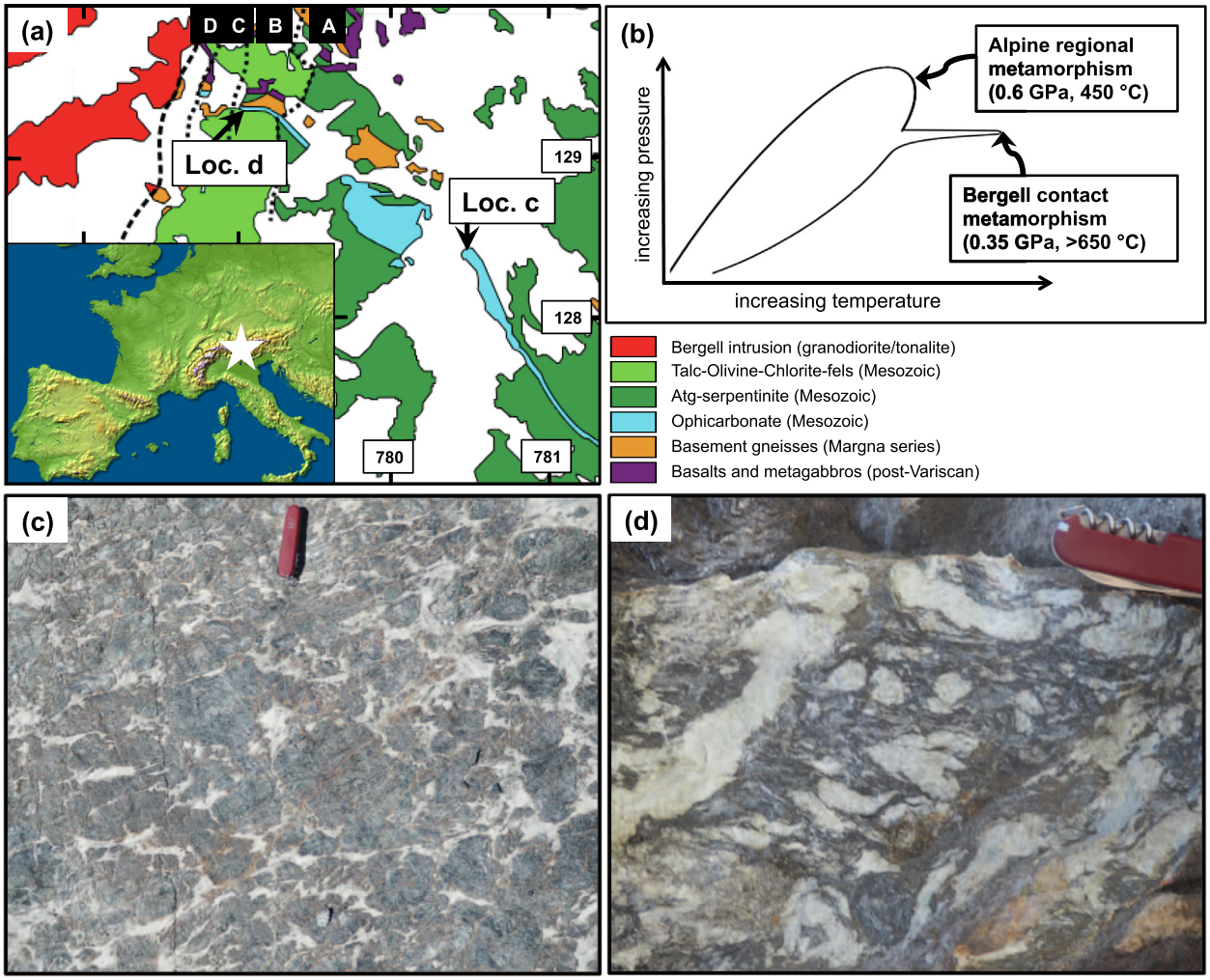


Fig. 1. (a) Geological sketch map illustrating the occurrence of Val Malenco ophicarbonates, with contact metamorphic mineral zones A to D in adjacent hydrous mantle rocks (simplified after Trommsdorff et al., 2005), (b) schematic P-T evolution of Alpine regional and contact metamorphism (peak temperature from this work), and ophicarbonate outcrop pictures of (c) Atg-ophicarbonate (mineral Zone A) and (d) Tr-ophicarbonate, carbonate-free (mineral Zone B), both localised in Fig. 1a.

reddish, Fe-bearing calcite is violet-blue, and Fe-bearing dolomite is blue-green, while dolomite, magnesite, and siderite remain colourless. The samples investigated in detail for this study are summarized in Table 1 and are part of the ~60 sample collection acquired during the field work campaigns.

Bulk compositions of meta-ophicarbonate samples were measured on pressed powder pellets by laser-ablation inductively-coupled-plasma mass-spectrometry (LA-ICP-MS), employing the procedures detailed in Peters and Pettke (2017). Rock samples of ~1 kg were crushed and pieces were comminuted in a steel mortar and pestle employing a hammer. The granular samples (<1 mm grain size) were then milled dry for 15 min in a planetary agate ball mill, to obtain a powder of ~25 μm average grain size. To reduce this average grain size by more than an order of magnitude, the sample was milled in water suspension for 30 min again in a planetary agate ball mill, the resulting slurry was transferred to Teflon beakers and dried on a hot plate overnight at 70 °C. 120 μg of dry powder was homogenised with 30 μg of microcrystalline cellulose with an agate mortar and pestle for 10 min by hand and then pressed to 10 mm diameter pellets applying 4 tonnes for 10 min, to be ready for LA-ICP-MS measurement.

LA-ICP-MS was used for bulk rock pressed powder pellets and for mineral trace element measurements on the same samples measured by electron probe microanalysis (EPMA; see below). The measurements were performed with a Geolas Pro 193 nm ArF Excimer laser (Lambda Physik, Germany) coupled with an ELAN DRCe quadrupole mass spectrometer (QMS; Perkin Elmer, USA) housed at the Institute of Geological Sciences, University of Bern. The laser system is characterized by a laterally homogeneous energy distribution, tuned to an ablation rate of about 0.15 μm per laser pulse (at energy densities of around 5 J/cm$^2$). A custom-built 20 cm$^3$ ablation cell was used, and the aerosol carrier gas was a He-$H_2$ mixture. The analytical set-up was tuned for optimum performance across the entire mass range. Daily optimization of the analytical conditions were done to satisfy a ThO production rate of below 0.2% (i.e., Th/ThO intensity ratio >500) and to achieve robust plasma conditions monitored by a Th/U sensitivity ratio of 1 as determined on the SRM612 glass standard. Measurements were done using 10 Hz laser repetition rate and 24–120 μm beam sizes, the maximum possible chosen for inclusion-free mineral domains to minimize limits of detection (LOD), while the pressed powder pellets were all ablated with a 120 μm beam.

External standardization was done employing GSD-1G from USGS (basalt glass doped with trace elements) with preferred values reported in Peters and Pettke (2017), and bracketing standardization provided a true-time linear drift correction. Internal standardization employed the sum of major element oxides minus wt% $H_2O + CO_2$ as determined by loss on ignition (LOI) for bulk rocks.

Data reduction was done off-line with the SILLS program (Guillong et al., 2008), with stringent LODs calculated for each element in every measurement following the formulation detailed in Pettke et al. (2012). Quality control was done using the harzburgite standard MUH-1 (Table A-1). Mean values of 6 spot measurements per LA-ICP-MS measurement session, normalised to reference values reported in Peters et al. (2017), cluster around 1. The standard deviation is less than 20% of the mean measured values except for Li, B, Cr, Ni, Zr, Mo, and Ta (Table A-1).

In-situ mineral measurements were done on polished sections of 50–70 μm thickness. Major to minor element data were acquired by EPMA, performed on a JEOL JXA-8200 electron probe at the Institute of Geological Sciences, University of Bern. The acceleration voltage was 15 kV. Beam current and diameter were optimised for the individual minerals as follows. For tremolite, diopside, and olivine the beam current was 20 nA and the beam diameter 3 μm. For antigorite and chlorite a current of 10–20 nA and a beam diameter of 4–10 μm was used. Carbonates were measured with a current of 4–5 nA and a diameter of 5 to 10 μm. Standards for quantitative analysis were minerals and synthetic oxides. A PhiRhoZ routine was used for matrix correction. Trace element data were measured by LA-ICP-MS employing the procedures detailed above. Internal standardisation for data quantification employed major element concentrations either determined

Table 1
Meta-ophicarbonate samples with mineral modes (vol%) employed in this study. Mineral abbreviations after Whitney and Evans (2010).

| Sample | Coordinates (WGS84) | Atg | Chl | Ol | Di | Tr | Cal | Dol | Opq | Lz | Ti-Chu | Tlc |
|---|---|---|---|---|---|---|---|---|---|---|---|---|
| **Zone A: Atg-ophicarbonates** | | | | | | | | | | | | |
| MAL_1523 | 46° 16.899′/9° 46.941′ | 50 | <1 | 3 | | 17 | 25 | | 5 | | | |
| MAL_1525 | 46° 16.890′/9° 46.883′ | 25 | 5 | | 5 | 10 | 50 | <5 | 3 | | | |
| MAL_1528 | block field 46° 17.462′/9° 45.894′ | 30 | <1 | 15 | 5 | 10 | 35 | <5 | <1 | | | |
| MAL_1503 a/b | 46° 16.939′/9° 46.498′ | 30 | | <5 | <1 | 5 | 60 | | <1 | | | |
| MAL_1505 | 46° 17.214′/9° 46.406′ | 20 | | <5 | <5 | 10 | 20 | 40 | 5 | | | |
| **Zone B: Tr-ophicarbonates** | | | | | | | | | | | | |
| MAL_1602 | block field below 1601 | <1 | 10 | 10 | | 55 | | 20 | <5 | | | |
| MAL_1601 | 46° 17.482′/9° 45.844′ | <1 | 10 | 20 | | 65 | | | 3 | <1 | <1 | |
| MAL_1608 a/b/c | Block field 46° 17.588′/9° 45.480′ | <5 | 10 | 30 | | 50 | | | <1 | | <1 | 5 |
| **Zone C: Di-ophicarbonates** | | | | | | | | | | | | |
| MAL_1612a | 46° 17.547/9° 45.565′ | <1 | 15 | 10 | 30 | <1 | 40 | | 5 | <1 | | |
| MAL_1610a | 46° 17.558′/9° 45.529′ | <1 | <1 | 20 | 15 | 5 | 50 | | 10 | | | |

by EPMA or the sum of major element oxides minus ($CO_2 + H_2O$) as derived from stoichiometry.

## 4. RESULTS

### 4.1. Petrography

Three distinct prograde mineral zones (A, B, C; Fig. 1a) can be distinguished in the field based on their mineral assemblages: Antigorite-ophicarbonate (Atg-ophicarbonate; Fig. 1c), tremolite-ophicarbonate (Tr-ophicarbonate; Fig. 1d), and diopside-ophicarbonate (Di-ophicarbonate). Meta-ophicarbonate samples were collected along a profile of increasing temperature across the Alpine contact aureole. All the Atg-ophicarbonate samples belong to ophicarbonate bodies in direct contact with large Atg-serpentinite masses. Outcrops of Tr-ophicarbonate were found within 20 metres of the contact to Margna gneisses, and abundant boulders occur in a scree. Di-ophicarbonate samples were collected at one cliff on the slopes of Valle Sissone. Rocks display highly heterogeneous deformation and modal carbonate/silicate ratios, at both outcrop and thin section scales, and meta-ophicarbonates are often matrix-supported. Common to the different meta-ophicarbonate rocks are a high abundance of inclusions in silicates except for tremolite, the presence of opaque minerals (dominantly magnetite as is characteristic for orogenic serpentinites; Piccoli et al., 2019), and variable but commonly prominent extents of retrogression, often showing late serpentine or talc along cracks and columnar tremolite overgrowing diopside in Di-ophicarbonate from zone C close to the intrusion.

#### *4.1.1. Zone A: Antigorite-ophicarbonate*

In outcrop, massive ophicarbonate textures consist of Atg-serpentinite fragments embedded in a carbonate matrix (Fig. 1c) that comprises between 20 and 80% of the rock. Serpentinite fragments are mm to several m large and partially aligned along a regional foliation. Textures within the clasts display a variably prominent local foliation cut by the carbonate matrix (Fig. 2a). Internal clast textures and overall rock foliation thus do not always coincide.

Atg-ophicarbonate consists of antigorite, tremolite, relic and metamorphic diopside, chlorite, calcite, subordinate dolomite, rare metamorphic olivine, and opaque minerals, representing regional metamorphic conditions without contact metamorphic overprint. Contacts between Atg-serpentinite clasts and carbonate matrix are sharp (Fig. 2a). In serpentinite domains relic and metamorphic diopside grains along with rare metamorphic xenomorphic olivine (note that metamorphic diopside and olivine are extremely hard to distinguish microscopically) are aligned along the antigorite matrix foliation. Relic diopside has a dusty appearance and contains opaque inclusions, in places likely tracing former orthopyroxene magmatic exsolution lamellae, and it is often overgrown by clear metamorphic diopside (Fig. 2b). Tremolite occurs in some samples, either showing long columnar single crystals or short columnar monomineralic aggregates preferably along the carbonate - silicate interface or as rare individual crystals within the antigorite matrix. Matrix tremolite crystals sometimes contain opaque inclusions, tracing the outline of former grain boundaries, similar to textures observed in diopside.

Carbonate types distinguished by thin section colourisation and confirmed by EPMA and LA-ICP-MS measurements reveal dominant calcite (0.5–3 mm grain size), displaying equilibrium texture (120° triple junctions) with subordinate interlocked grain boundaries (Fig. 2a). Domains of fine-grained carbonate, partially also with palisade-like texture, coexist with domains of coarse-grained carbonates at centimetre scale. Iron-free calcite dominates, iron-bearing calcite and dolomite are subordinate and not observed in all samples.

Opaque minerals comprise magnetite and sulphides (0.01–1 mm in size; not further differentiated) and mostly occur within the serpentinite domain (Fig. 2a). Magnetite modally dominates over sulphides. Opaque minerals are often arranged along the internal foliation of the serpentinite fragments, some are also related to tremolite grains or tremolite aggregates, and they also occur within the carbonate domain as inclusions or along grain boundaries.

#### *4.1.2. Zone B: Tremolite-ophicarbonate*

A ductile deformation texture between olivine-chlorite ± tremolite domains (dark) and near-monomineralic tremolite domains (white) prevails. Tr-ophicarbonate largely preserves the former ophicarbonate texture, both at outcrop (Fig. 1d) and in thin section (Fig. 2c) scales, displaying sharp boundaries between former serpentinite clasts and carbonate matrix at all scales.

Tr-ophicarbonate consists of tremolite, olivine, chlorite, and minor to no carbonate, along with retrograde serpentine (interpreted to be colourless antigorite) and traces of talc. Opaque minerals (magnetite with traces of sulphides) are also present. In former Atg-serpentinite clasts, fractured olivine grains (up to 5 mm in size) are associated with individual idiomorphic, columnar tremolite crystals of up to 1 mm in size or with radial tremolite aggregates, with chlorite (brownish anomalous interference colours), and minor opaque minerals (Fig. 2c). Some domains show an equilibrium texture made up of equigranular olivine grains smaller than 0.5 mm associated with tremolite and subordinate chlorite. Fractures in olivine crystals or zones along grain boundaries are partially filled with felty, yellowish serpentine lined with magnetite, interpreted to represent low-T retrograde chrysotile/lizardite + magnetite crystallisation. Vein-type domains (<2 mm thick) along grain boundaries consist of fine-grained aggregates of antigorite (colourless in plane-polarised light) along with talc and/or tremolite.

Former ophicarbonate matrix now consists of clear, idiomorphic, monomineralic tremolite domains with minor opaque minerals (Fig. 2d). Bulk rock tremolite modes observed in the field often exceed 50%. Dolomite and rare calcite are sometimes observed along with tremolite in samples with originally >70% former carbonate matrix as estimated from rock texture.

#### *4.1.3. Zone C: Diopside-ophicarbonate*

The few outcrops in zone C consist of monomineralic carbonate alternating with silicate domains showing gradual contacts between the two. Mineral assemblages consist

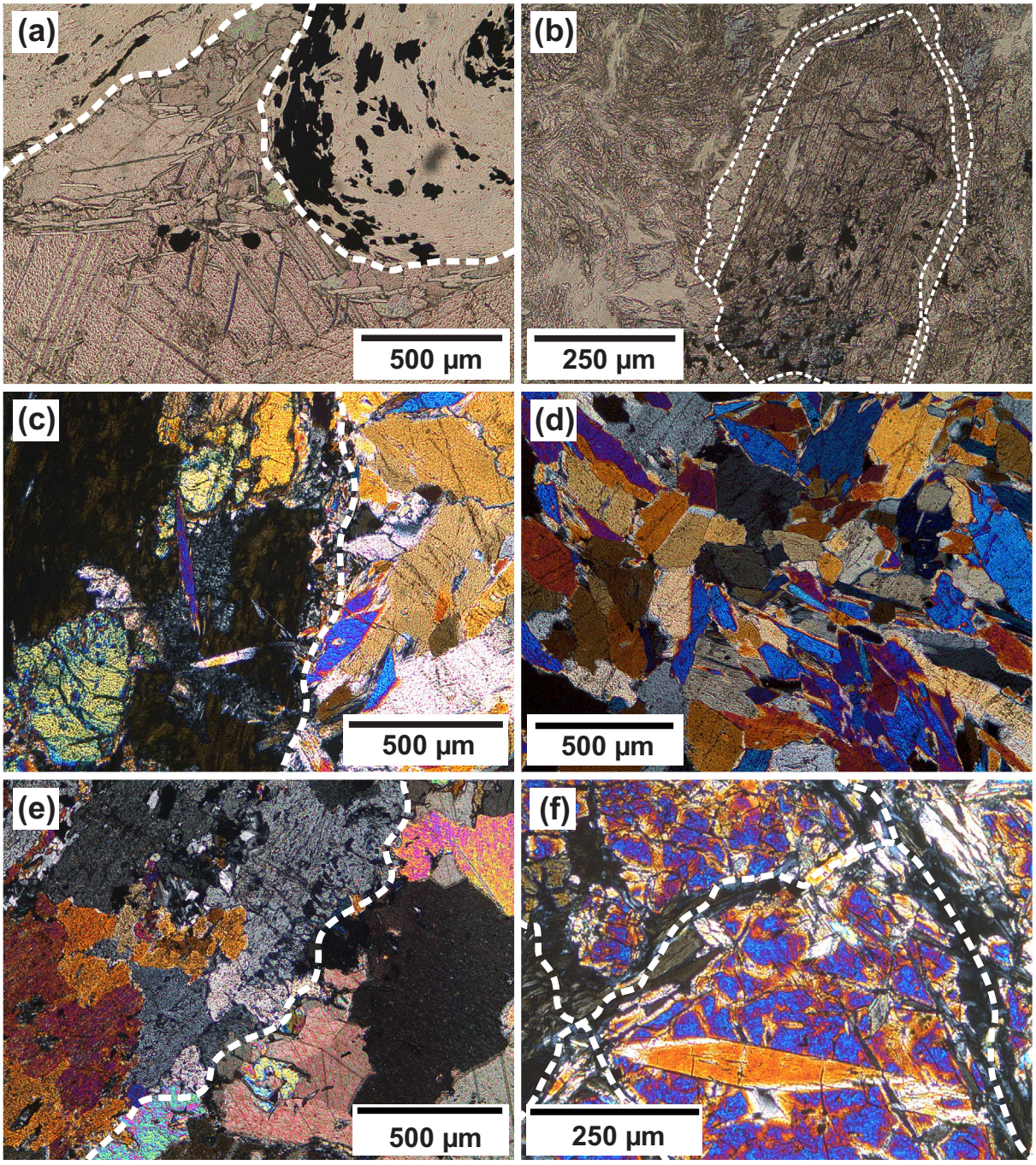


Fig. 2. Thin section images (a), (b) taken at plane polarised light, (c) to (f) with crossed polarisers. (a) Atg-ophicarbonate. Sharp borders (white dashed line) between Atg-serpentinite and calcite matrix showing typical twinning. The reddish calcite colour originates from thin section carbonate colourisation (sample MAL_1503b). (b) Atg-ophicarbonate. Relic clinopyroxene displaying cleavage with metamorphic rim in tremolite-bearing Atg-serpentinite clast (sample MAL_1528). (c) Tr-ophicarbonate. Former Atg-serpentinite clast to the left now consisting of olivine and chlorite (dark brown) and former calcite matrix to the right now consisting of near monomineralic tremolite. Two tremolite blades overgrow the olivine-chlorite part (sample MAL_1601). (d) Tr-ophicarbonate. Equilibrium texture monomineralic tremolite in former ophicarbonate calcite matrix (sample MAL_1601). (e) Di-ophicarbonate. Diopside full of inclusions to the left of the white dashed line is in sharp contact with blocky twinned calcite (sample MAL_1612a). (f) Di-ophicarbonate. Retrograde tremolite blades overgrowing diopside associated with chlorite (brown interference colours). Fracture-related retrogression to serpentine (gray interference colours) is traced by white dashed lines (sample MAL_1612d). (For interpretation of the references to colour in this figure legend, the reader is referred to the web version of this article.)

of diopside, olivine, chlorite, and calcite, along with retrograde serpentine (interpreted as antigorite because it is colourless in plain polarised light), and opaque minerals (magnetite dominates over sulphides; however, sulphides tend to be more abundant than in zones A and B).

Silicate domains are characterised by millimetre-sized diopside displaying locally a spinifex-type texture. Crystals appear dusty in thin section (Fig. 2e) because they are full of inclusions (carbonate, chlorite, ±opaque minerals) and variably fractured, the fractures often filled with a felt of retrograde colourless serpentine (Fig. 2f). Rarely, spinifex-textured diopside is rimmed by small, clear diopside overgrowths showing equilibrium texture along with equigranular (up to 0.5 mm in size), inclusion-free, small olivine crystals. Chlorite either rims opaque minerals or is associated with diopside crystals.

Carbonate domains consist of 1–2 mm large calcite grains with polygonal texture (Fig. 2e). Olivine, diopside, minor chlorite, and opaque minerals are observed along the calcite grain boundaries and sometimes as inclusions in calcite.

Tremolite (confirmed by RAMAN spectroscopy) was observed in some samples, notably overgrowing spinifex-textured diopside (Fig. 2f), indicating retrograde formation. The crystals are either idiomorphic single columnar crystals or grew in unoriented, monomineralic aggregates.

#### 4.1.4. Zone D: Spinel-ophicarbonate

Meta-ophicarbonate in zone D producing spinel at the expense of chlorite (as predicted by thermodynamic calculations; see below) was not observed in the field (note that the intrusion contact is buried beneath a scree; Fig. 1a).

### 4.2. Compositional data

All measurement data are reported in Tables A-1 to A-7 (electronic supplementary material A) and illustrated in Figs. 3–9. Bulk rock data are followed by in-situ mineral data for antigorite, carbonates, tremolite, diopside, olivine, and chlorite.

#### 4.2.1. Bulk rock

Bulk rock major element meta-ophicarbonate data (Table A-1) primarily reflect the variable mixtures between serpentinite and calcite (Fig. 3), with CaO concentrations ranging between 6.8 and 37.1 wt%. Fig. 3 further illustrates that our data for Atg-ophicarbonate fall in the binary mixing field of ocean floor serpentinite and calcite, as do most of the data for obducted ocean floor ophicarbonate from the Internal Ligurides representing former Piemont-Ligurian ocean floor (Cannaò et al., 2020) and data for high-P metamorphic ophicarbonate from Almirez (Menzel et al., 2019). Data for Tr-ophicarbonate samples are displaced from the binary mixing field towards the measured tremolite compositions, while data for Di-ophicarbonate samples are also slightly displaced towards higher $SiO_2$/MgO (at given Ca).

Bulk rock $FeO_{tot}$ (representing total measured Fe expressed as FeO due to absence of measurement data for $Fe^{3+}$) vs. MgO reveals that magnesium numbers

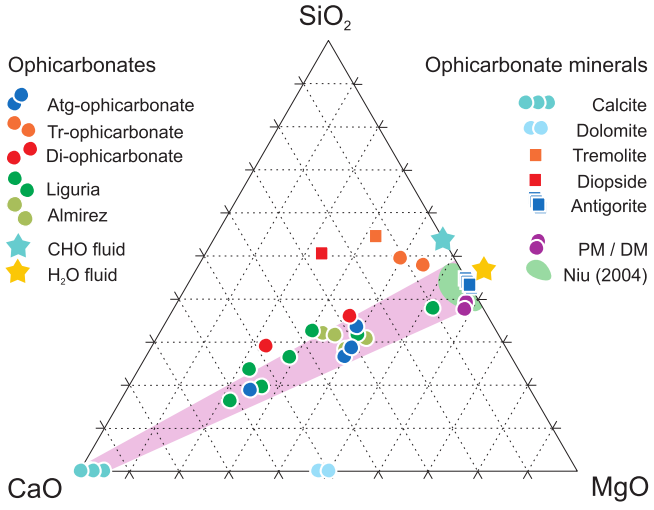


Fig. 3. Molar ternary plot. Atg-ophicarbonate (Zone A), Tr-ophicarbonate (Zone B), and Di-ophicarbonate (Zone C) bulk rock data from this work compared to data for oceanic (Liguria; Cannaò et al., 2020) and high-P metamorphic (Cerro del Almirez; Menzel et al., 2019) ophicarbonate. Niu (2004) refers to dredged, serpentinised abyssal peridotites. Primitive mantle (PM; Palme and O'Neill, 2004) and depleted mantle (DM; Salters & Stracke, 2004) for reference of the non-hydrated peridotite component of ophicarbonate. The pink field encloses binary mixtures between ocean floor serpentinites (light green field; data from Niu, 2004) and calcite. Stars for $H_2O$ fluid (displaced to the right of the MgO-$SiO_2$ join for visibility) and CHO fluid represents measured solute load in experimental fluids (800 °C/1 GPa) in the systems MgO–$SiO_2$–$H_2O$ and MgO–$SiO_2$–CHO, respectively (Tumiati et al., 2017). Note the displacement of notably the Tr-ophicarbonate data towards $SiO_2$ and away from the CaO corner, rocks that are inferred to have contained 30–50% calcite in the starting ophicarbonate (compare Fig. 1d). (For interpretation of the references to colour in this figure legend, the reader is referred to the web version of this article.)

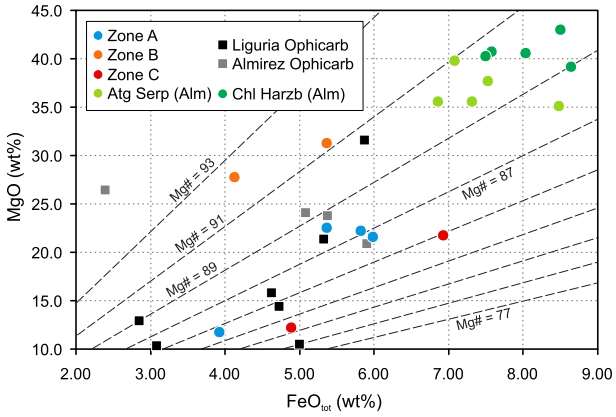


Fig. 4. Bulk rock ophicarbonate $FeO_{tot}$ vs MgO plot contoured for Mg#. Zone A: Atg-ophicarbonate, Zone B: Tr-ophicarbonate, Zone C: Di-ophicarbonate, compared to oceanic (Liguria; Cannaò et al., 2020) and high-P metamorphic (Cerro del Almirez; Menzel et al., 2019) ophicarbonate. Antigorite-serpentinite and chlorite-harzburgite data from Almirez (Bretscher et al., 2018) for reference to metamorphic hydrated mantle rocks. Note the large range in Mg# of oceanic and metamorphic ophicarbonate when compared to metamorphic hydrous mantle rocks. (For interpretation of the references to colour in this figure legend, the reader is referred to the web version of this article.)

(Mg# = 100*[MgO/(MgO + $FeO_{tot}$)]$_{molar}$) range considerably between 82 and 92, whereby Tr-ophicarbonate samples show higher, and Di-ophicarbonate samples lower, values than associated Atg-ophicarbonate samples (Fig. 4). However, the range in our data corresponds to that reported for Ligurian ocean floor and Almirez high-P ophicarbonate and is prominently larger than that typically displayed by Atg-serpentinite and their partially dehydrated Chl-harzburgite equivalents (data from Bretscher et al., 2018, for comparison). $Al_2O_3$ contents are below the primitive mantle (PM) value of 4.5 wt% (Palme and O'Neill, 2004). Of the transition metals, Ni and Cr are of the order of several hundreds to 2500 µg $g^{-1}$ as is typical for mantle rocks, except for Tr-ophicarbonate sample MAL_1601

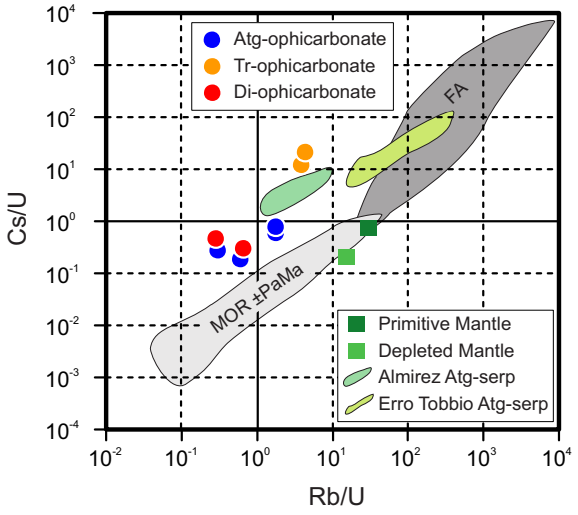


Fig. 6. Trace element discrimination diagram employing elements that show very low concentrations in calcite (the main carbonate mineral in the metamorphic ophicarbonate; Table A-3), in order to compare the different meta-ophicarbonate types of this work with ocean floor serpentinite formation domains (MOR = Mid Ocean Ridge; PaMa = Passive Margin; FA = Forearc; Peters et al., 2017) and orogenic antigorite serpentinites from Almirez (Peters et al., 2017) and Erro Tobbio (Peters et al., 2020). Note the slight relative enrichment of Tr-ophicarbonate in alkali elements that may indicate aqueous fluid infiltration driving $CO_2$ mobilisation. Meta-ophicarbonate sample colour coding according to Fig. 3. Primitive and depleted mantle values from Palme and O'Neill (2004). (For interpretation of the references to colour in this figure legend, the reader is referred to the web version of this article.)

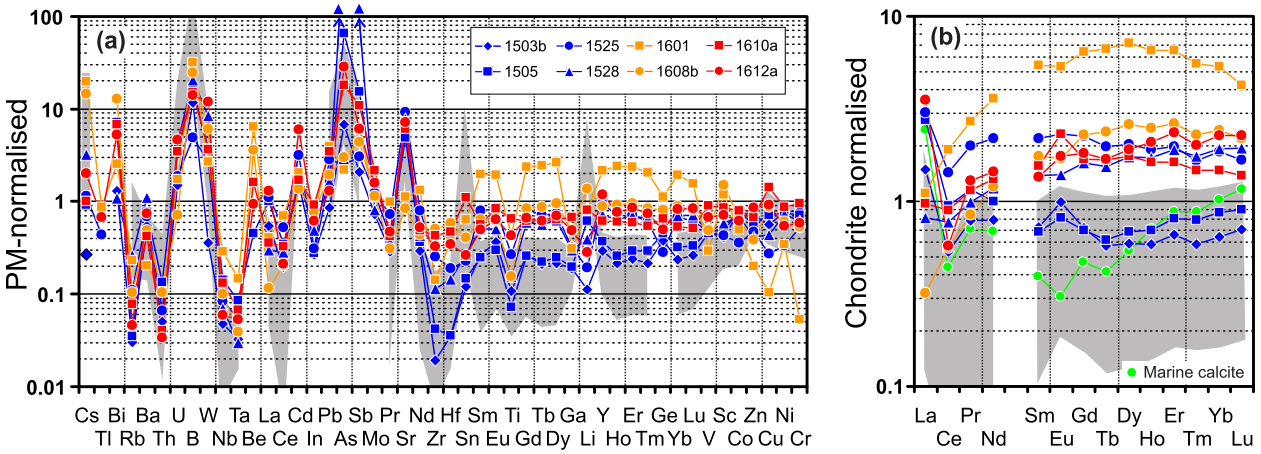


Fig. 5. (a) Primitive mantle (PM) normalised bulk rock trace element diagram and (b) chondrite-normalised REE patterns. Meta-ophicarbonate types are colour-coded, with blue for Atg-ophicarbonate (zone A), orange for Tr-ophicarbonate (zone B) and red for Di-ophicarbonate (zone C). The gray band in (a) and (b) represents obducted ocean floor ophicarbonate of the Internal Ligurides (Cannaò et al., 2020). Marine calcite data, green dots, in (b) represent fibrous calcite cement precipitated from Jurassic seawater (Della Porta et al., 2015). PM values after Palme and O'Neill (2004). (For interpretation of the references to colour in this figure legend, the reader is referred to the web version of this article.)

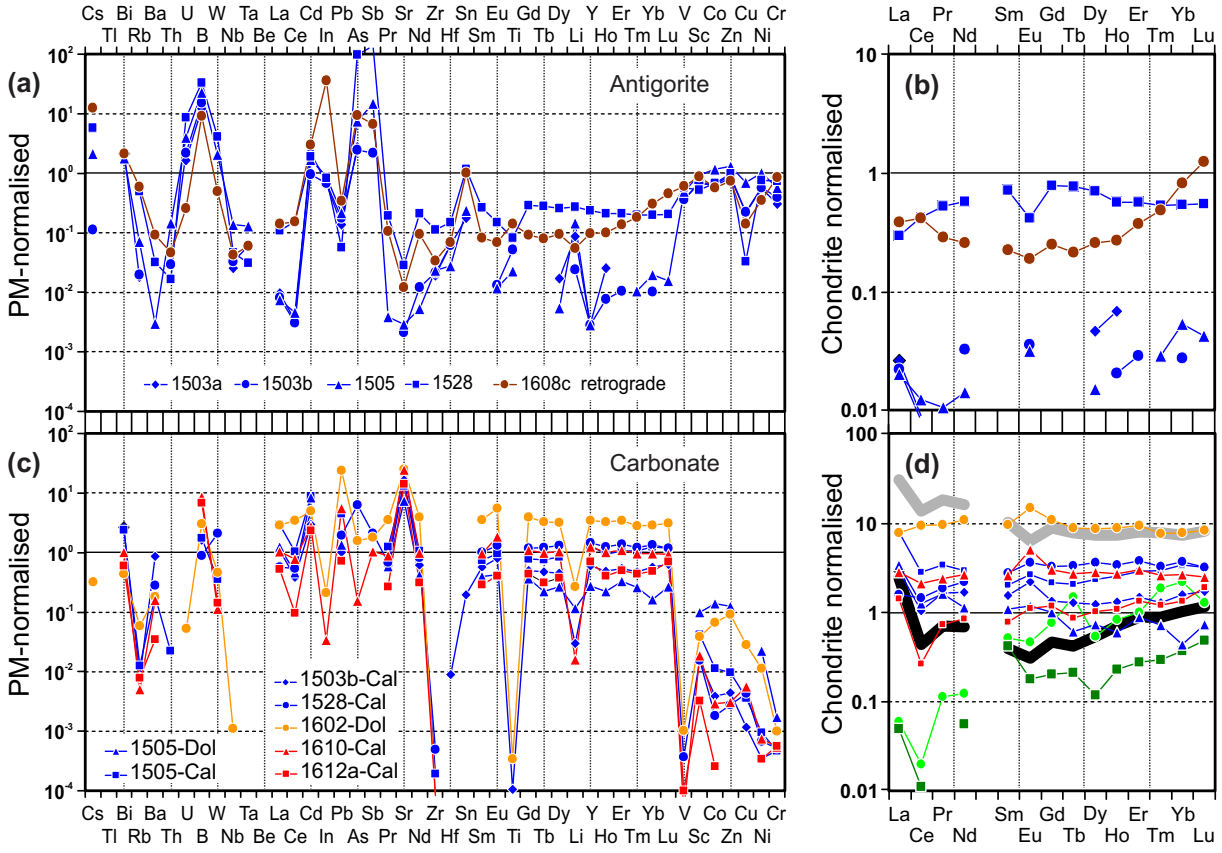


Fig. 7. (a) and (c) Primitive mantle (PM) normalised antigorite and carbonate trace element diagrams and (b) and (d) chondrite-normalised REE patterns. In figure (d) are given for comparison (i) modern Eastern North Atlantic seawater data from station O: 57.15 °N, 9.70 °W, 1916 m depth (Crocket et al., 2018) multiplied by $10^6$ in gray thick line, (ii) average data for fibrous calcite cement precipitated from Jurassic seawater (Della Porta et al., 2015) in black thick line, and (iii) average clast (light green) and vein (dark green) calcite data for obducted ocean floor ophicarbonate of the Internal Ligurides (Cannaò et al., 2020). Meta-ophiolite sample type colour coding according to Fig. 3. (For interpretation of the references to colour in this figure legend, the reader is referred to the web version of this article.)

(zone B) that has comparatively low contents of Cr = 140 and Ni = 680 μg $g^{-1}$, respectively.

REE in chondrite-normalised representation (Fig. 5b) reveal overall flat patterns. Two Tr-ophicarbonate samples are characterised by $LREE_N \ll MREE_N > HREEN$ and a slight negative Eu anomaly ($Eu/Eu^* = Eu_N \times (Sm_N + Gd_N)^{0.5}$) along with a slight positive Ce anomaly ($Ce/Ce^* = Ce_N \times (La_N + Pr_N)^{0.5}$), while all other samples have $MREE_N \sim HREE_N$ and tend to have a positive Eu anomaly. Conspicuous is their variably prominent La enrichment of up to $La_N = 2.7*Pr_N$ along with a variably negative Ce anomaly of between 0.27 and 0.86.

Trace element variations are illustrated in Fig. 5a in a primitive mantle (PM) normalized diagram. Variably prominent positive anomalies are apparent for B, U, As, Sb, Bi, Cs, W, Ba, Cd, and Sr; hence, the meta-ophicarbonates show the element enrichments characteristic of peridotites hydrated on the ocean floor including those in passive margin settings (e.g., Kodolányi et al., 2012; Peters et al., 2017). Again, Tr-ophicarbonate samples stand out by having the highest Cs, B, and Be enrichments, along with moderate enrichments in As, Sb, and Sr. All samples display variably prominent U enrichments ($7 < U_N/Th_N < 140$) as is typical for oceanic serpentinites formed near the ocean floor surface.

A trace element discrimination diagram (Fig. 6) developed for oceanic serpentinites (Peters et al., 2017) may help to assess the environment of dominant rock hydration, given the observation that Cs, Rb, and U used in this diagram show very low concentrations in calcite of Atg-ophicarbonate. Atg-ophicarbonate (and Di-ophicarbonate) samples show Cs/U abundance ratios indistinguishable from mantle values along with much lower Rb/U ratios. When compared to oceanic serpentinites from mid ocean ridge/passive margin and forearc settings, Rb/U of Atg- and Di-ophicarbonates overlap with average mid ocean ridge serpentinites while their Cs/U ratios are at the higher end of the mid ocean ridge range. The Tr-ophicarbonate samples possess Rb/U still overlapping with mid ocean ridge data; however, their Cs/U is significantly elevated and within the range reported for forearc serpentinites. These signatures are largely comparable with those of orogenic serpentinites from Almirez (Peters et al., 2017) while those of Erro Tobbio possess distinctly higher relative alkali element contents, more consistent with forearc serpentinisation (compare Peters et al., 2020). All Tr-

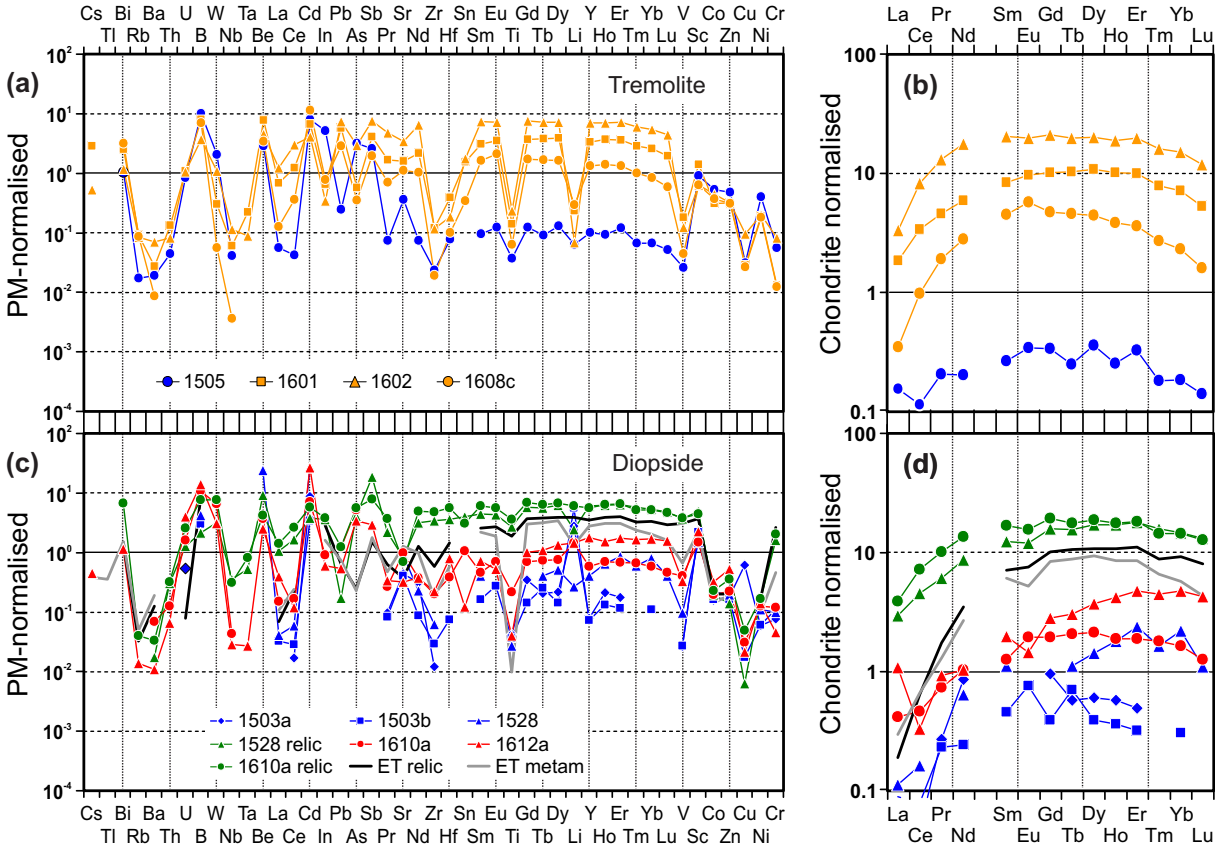


Fig. 8. (a) and (c) Primitive mantle (PM) normalised tremolite and diopside trace element diagrams and (b) and (d) chondrite-normalised REE patterns. Relic and metamorphic diopside data from Erro Tobbio (ET) orogenic serpentinites (Peters et al., 2020) are displayed in (c) and (d) for comparison. Meta-ophiolite sample type colour coding according to Fig. 3. (For interpretation of the references to colour in this figure legend, the reader is referred to the web version of this article.)

ophicarbonate samples (zone B) show elevated Cs/U ratios along with less prominently depleted Rb/U, going along with less prominent U enrichment (compare Table A-1). We note that notably Cs and Rb are prone to fluid-mediated modification upon progressive devolatilisation reactions, to be discussed below.

*4.2.2. Minerals*

Data are presented per mineral along increasing temperature (mineral zones A to C) progressively approaching the intrusion contact. Retrograde minerals are only included in this description where relevant.

*4.2.2.1. Antigorite.* Prograde regional metamorphic antigorite is the major silicate constituent in mineral zone A and has $Al_2O_3$ concentrations ranging between 1.2 and 3.7 wt% (Table A-2), overlapping with those in Atg-serpentinites of Val Malenco (Zihlmann, 2012) and other orogenic serpentinites. Iron contents are variable, ranging between 3 and 8 wt% $FeO_{tot}$. The corresponding Mg# vary between 0.88 and 0.96, and samples with lower Fe-contents also have less $Al_2O_3$ and $Cr_2O_3$. When compared to Atg-serpentinites (Zihlmann, 2012), $Cr_2O_3$ contents in antigorite of the meta-ophicarbonate are distinctly lower. Fluid mobile element (FME) enrichment patterns of antigorite (Fig. 7a) largely correspond to those seen for bulk meta-ophicarbonate rocks (Fig. 5a), notably for B, W, As, Sb, Cd, and prominently elevated U/Th; thus documenting that antigorite is the main host for these hydration-related FME enrichments. REE patterns (Fig. 7b) tend to be hump-shaped, with $LREE_N \ll MREE_N > HREE_N$, and display the positive La anomaly in low-concentration samples as seen for bulk ophicarbonate rocks.

Retrograde antigorite (interpreted as such because it is colourless) consists of two types, one showing elevated MgO along with reduced $SiO_2$ (both correlating negatively) and ~8 wt% $Al_2O_3$ and ~6 wt% $FeO_{tot}$ (Table A-2), thus indicating antigorite + brucite ± chlorite (±magnetite) sub-microscopic intergrowths. The second type is $SiO_2$ enriched (~48 wt%), has MgO around 32 wt%, about 4 wt% $Al_2O_3$ and 4 wt% $FeO_{tot}$, thus again suggesting intergrown hydrous silicates, possibly chlorite – talc enriched. Their REE pattern (Fig. 7b) is U-shaped and thus different from prograde antigorite, while trace element distribution patterns of the different retrograde antigorite types are largely identical and correspond well to that of prograde antig-

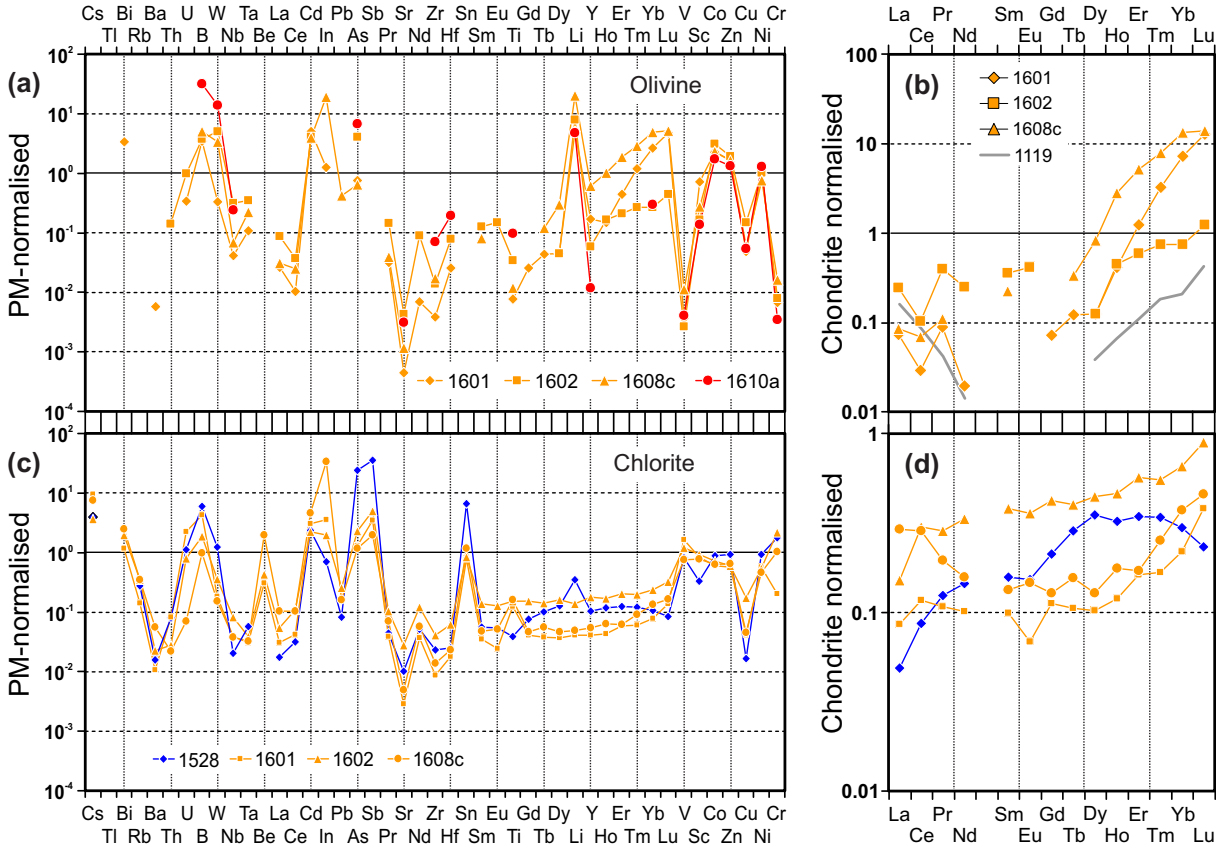


Fig. 9. (a) and (c) Primitive mantle (PM) normalised olivine and chlorite trace element diagrams and (b) and (d) chondrite-normalised REE patterns. An olivine REE pattern from Val Malenco Atg-serpentinite (gray line, sample MAL_1119; Zihlmann, 2012) is given in (b) for comparison. Meta-ophiolite sample type colour coding according to Fig. 3. (For interpretation of the references to colour in this figure legend, the reader is referred to the web version of this article.)

orite, with the $SiO_2$-rich types showing overall lower trace element contents; therefore, the grand average is displayed for retrograde antigorite in Fig. 7a.

*4.2.2.2. Carbonates.* Carbonate is dominantly calcite with subordinate dolomite (Table A-3). Dolomite contains higher FeO contents of up to 2.2 wt% (calcite in Atg- and Tr-ophicarbonate is always <0.33, and <0.1 in Di-ophicarbonate). Calcite displays low MgO and FeO along with distinct Sr and B positive anomalies and variably elevated Ba, Bi, W, and Pb, while other ocean floor hydration-related FME like U, As, Sb are variably low (Fig. 7c). Importantly, U and Th measurements were commonly below the respective LODs down to 1 ng $g^{-1}$, thus revealing that it is the silicates and not the carbonates that host the U enrichments measured for bulk rocks. Dolomite and calcite trace element patterns in Atg-, Tr-, and Di-ophicarbonates are overall identical, at concentrations that vary by up to an order of magnitude, however. Dolomite coexisting with calcite in Atg-ophicarbonate (sample MAL_1505) shows overall lower trace element contents including the carbonate-characteristic FME and the lowest REE (subchondritic HREE), while most transition metals are enriched in dolomite. Calcite REE patterns are overall flat, while dolomite in Atg-ophicarbonate has $LREE_N > HREE_N$ (Fig. 7d). Both carbonates show in part a prominent La enrichment (up to $La_N = 2.3*Pr_N$), and a variably negative Ce anomaly of between 0.47 and 0.85. Notably the LREE pattern of the carbonates (Fig. 7d) largely mirrors that for modern 1900 m deep Eastern North Atlantic seawater (Crocket et al., 2018) and of calcite precipitated from Jurassic seawater (Della Porta et al., 2015) except for its negative Eu anomaly. Data for calcite of obducted oceanic ophicarbonate from the Internal Ligurides (Cannaò et al., 2020) are also comparable except that they have lower LREE concentrations.

*4.2.2.3. Tremolite.* Tremolite is stable in Atg- and Tr-ophicarbonate, and its compositions vary as a function of textural positions (Table A-4; Fig. 8a, b). In Atg-ophicarbonate, tremolite crystallised along the carbonate - silicate interface (sample MAL_1525) shows lower Mg# of ~92.5 than tremolite dispersed throughout the Atg-serpentinite matrix (sample MAL_1528; Mg# ~95.7). Tremolite in Tr-ophicarbonate constitutes the major silicate and has a Mg# varying between 93.4 and 95.7. Contents of $Al_2O_3$, Cr, and Ni tend to be higher in tremolite of Atg-ophicarbonate than of Tr-ophicarbonate. Smooth

REE patterns of tremolite are variably pronounced hump-shaped with $MREE_N > HREE_N$ and $MREE_N \gg LREE_N$, and concentrations are more than an order of magnitude lower for tremolite in Atg-ophicarbonate when compared to Tr-ophicarbonate (Fig. 8b). Their trace element distribution patterns are largely identical (e.g., for the incompatible elements and the transition metals), notably including pronounced positive anomalies in B, Bi, U, W, Cd, and also Be (Fig. 8a).

*4.2.2.4. Diopside.* Diopside (Table A-5) occurs in Atg-ophicarbonate as relic and metamorphic and in Di-ophicarbonate as the major silicate mineral along with prominent olivine. Relic diopside (Fig. 2b) occurs in both Atg- and Di-ophicarbonate and is characterised by low Mg# (~91.5) along with elevated $Al_2O_3$ (up to 5 wt%), $Na_2O$ (up to 1.0 wt%) and $0.57 < Cr_2O_3 < 0.95$ wt%. It possesses hump-shaped REE spectra closely comparable to those of tremolite in Tr-ophicarbonate, albeit with less pronounced LREE and HREE depletions (Fig. 8d). These patterns closely compare to those reported for relic magmatic and metamorphic diopside from Erro Tobbio Atg-serpentinites (Peters et al., 2020; Fig. 8d).

Metamorphic diopside displays Mg# of up to 97.6 in Atg-ophicarbonate, while metamorphic diopside in Di-ophicarbonate has $87.6 < Mg\# < 95.5$, and all have significantly lower REE concentrations than relic diopside, with $LREE_N \ll HREE_N$. Comparison of the trace element distribution of relic and metamorphic diopside reveals an overall similar pattern with prominent enrichments in U, B, W, Be, Cd, and ±As, ±Sb (Fig. 8c). Exception to this uniformity are a negative Sr anomaly and higher incompatible HFSE and Cr concentrations in relic diopside while the Sr anomaly for metamorphic diopside is distinctly positive along with much lower incompatible HFSE and Cr concentrations, and diopside in Di-ophicarbonate displays variably enriched Ni relative to Cr.

*4.2.2.5. Olivine.* Olivine was measured in all meta-ophicarbonate types (Table A-6); however, trace element data for Atg-ophicarbonate (sample MAL_1503b) and Di-ophicarbonate (sample MAL_1610a) are only very few (Fig. 9a, b) because inclusion-free domains suitable for measurement were basically absent. A single olivine from Atg-ophicarbonate has a Mg# of 90.8 that overlaps with olivine of the adjacent Atg-serpentinites (Zihlmann, 2012). It is equal to (sample MAL_1612a; Mg# ~90.3) or slightly lower than for olivine from Di-ophicarbonate (Mg# ~93), while that for olivine from Tr-ophicarbonate ranges between 83.4 and 88.7 (4 samples and each sample showing a narrow range). All olivine types have very low $Al_2O_3$, CaO, $Na_2O$, $K_2O$, $TiO_2$ and $Cr_2O_3$ contents as is characteristic of metamorphic olivine. Olivine NiO contents ranges between 0.20 and 0.25 wt% in Atg- and Tr-ophicarbonate, while NiO contents are higher in Di-ophicarbonate (0.27–0.44 wt%).

Olivine REE patterns are only available for Tr-ophicarbonate, displaying $HREE_N \gg MREE_N$ and $MREE_N \sim LREE_N$ (Fig. 9b). These patterns largely coincide with olivine REE pattern of Atg-serpentinites (sample MAL 1119, Zihlmann, 2012). FME enrichments in olivine of both Tr- and Di-ophicarbonate display patterns typical of olivine formed upon antigorite dehydration (e.g., Scambelluri et al., 2014; Bretscher, 2017), displaying positive anomalies for B, W, As, Cd, In, and Li in most samples (Fig. 9a).

*4.2.2.6. Chlorite.* Chlorite in Atg-ophicarbonate displays low $Al_2O_3$ (~12.5 wt%) along with high NiO (>0.20 wt%) and $0.90 < Mg\# < 0.93$, sometimes displaying Fe-richer rims (Table A-7). Chlorite of Di-ophicarbonate has the highest Mg# of ~96 along with very high $Al_2O_3$ of ~20 wt%, while chlorite in Tr-ophicarbonate is variable in composition and lies generally in between the other two types. Chlorite REE patterns are hump-shaped for Atg-ophicarbonate ($LREE_N \ll MREE_N$ and $HREE_N < MREE_N$) but show a general concentration increase from HREE to LREE for chlorite of Tr-ophicarbonate ($LREE_N \sim MREE_N$ and $HREE_N > MREE_N$; Fig. 9d), with a tendency for a U-shaped pattern. FME patterns are largely identical for all chlorite-types, showing enrichments in Cs, Bi, U, B, W, Be, Cd, In, As, Sb, and Sn (Fig. 9c), closely comparable to enrichments observed for antigorite.

*4.2.2.7. Opaque minerals.* Opaque minerals were not further differentiated in this study. They comprise variable modes of magnetite (present in all our meta-ophicarbonate samples), along with variable and subordinate modes of pyrrhotite, pentlandite, and possibly other sulphides. Occasional presence of heazlewoodite, awaruite, and ilmenite has also been reported for adjacent Atg-serpentinites (Trommsdorff and Evans, 1977).

## 5. PHASE DIAGRAM CALCULATION

### 5.1. Strategy and settings

The fate of ophicarbonate with progressive devolatilisation was calculated using the free energy minimisation method. Devolatilisation reactions liberate large amounts of COH-fluids that escape and migrate through adjacent rocks. This can have major implications on the bulk rock composition at a certain location, since reactive fluid flow adds or removes matter. However, to simplify calculations all our models were done using constant composition and closed system conditions. Deviations of these closed-system models from our field observations are then discussed with respect to open-system equilibrium conditions. A detailed description of the modelling strategy can be found in the electronic supplementary material B.

The Perple_X software, version 6.7.7 (Connolly, 2005, with updates), was used together with the Holland and Powell database 2002 (Holland and Powell, 1998, with subsequent updates) and the CORK equation of state (Holland and Powell, 1991). PT- pseudosections were calculated for the 7 components system $SiO_2$ – MgO – $Al_2O_3$ – FeO – CaO – $H_2O$ – $CO_2$ (Fig. 10 and electronic supplementary material). Despite evidence for the presence of ferric iron in some minerals, e.g., antigorite, chlorite, and magnetite,

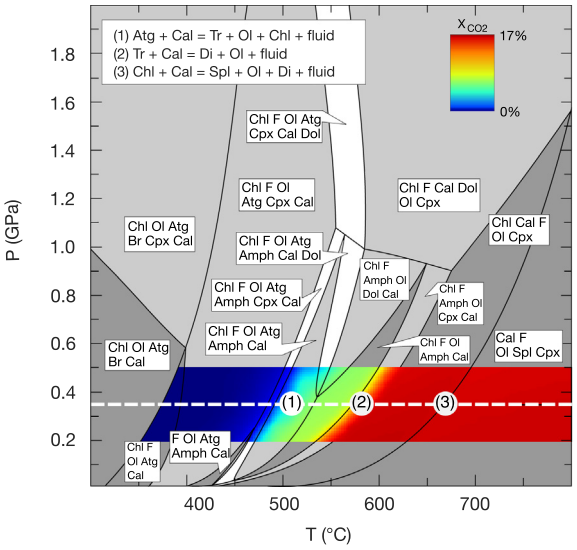


Fig. 10. Closed system equilibrium pseudosection for ophicarbonate (20 wt% calcite – 80 wt% serpentinite), with colour-coded $X_{CO2}$ of the rock-buffered mixed $H_2O$-$CO_2$ fluid. Dashed white line represents the path of isobaric heating upon contact metamorphism in response to the Bergell intrusion, with the major reaction numbers addressed in the text. Mineral abbreviation after Whitney and Evans (2010), and F stands for fluid. (For interpretation of the references to colour in this figure legend, the reader is referred to the web version of this article.)

ferric iron is excluded in our models since it is currently not possible to accurately calculate the ferric Fe content in antigorite, being a major phase at low temperature. Moreover, charged species in the fluid are also neglected, i.e., the fluid is modelled as a simple $H_2O$-$CO_2$ binary. The model ophicarbonate bulk compositions considered are mixtures of bulk silicate and variable amounts of $CaCO_3$ (Table B-1). The bulk silicate composition was modelled as an almost completely serpentinised harzburgite without diopside, taken from bulk rock data for Val Malenco Atg-serpentinites (Zihlmann, 2012), which is also in agreement with typical ocean floor serpentinite with significant melt depletion (e.g., Kodolányi et al., 2012). The bulk Si/Mg ratio in the carbonate-free system was set to absence of talc at low temperature prior to antigorite-out, consistent with field observations in regional metamorphic Atg-serpentinite mineral assemblages (Zihlmann, 2012). A fluid-saturated isobaric T-$X_{CO2}$ diagram on an 80 wt%:20 wt% bulk silicate:calcite mixture was calculated in order to illustrate the effects of an infiltrating low $X_{CO2}$ fluid on the mineral assemblages. Our approach is closely comparable to that chosen by Menzel et al. (2019) for higher pressures.

All minerals included are treated as solid solutions. Tschermak-substitution was only considered for the sheet silicates talc, antigorite, and chlorite since our EPMA data on metamorphic tremolite and diopside (Tables A-4 and A-5) do not indicate significant Al content ($Al_2O_3 < \sim 0.5$ wt%). This simplification does not modify the sequence of major dehydration reactions; however, continuous dehydration resulting from Al-exchange between chlorite and diopside in Tr-ophicarbonate prior to the spinel-in reaction is suppressed. A complete list of phases and solid solutions models employed is presented in Table B-2.tpb 2

### 5.2. Phase relations

In carbonate free hydrous peridotite systems the major equilibrium dehydration reactions are continuous with increasing temperature along increasing Mg# of the reactant hydrous silicates. At our low P conditions of 0.35 GPa these are, in prograde order, brucite-out, antigorite-out, talc-out, anthophyllite-out, and chlorite-out (Fig. B-1). Talc in hydrous peridotite is stable across a rather small temperature interval (~50 °C) above antigorite-out whose width depends on Si activity.

Relationships are different in ophicarbonate, for which a pseudosection is illustrated in Fig. 10. The mineral modes are given in Fig. 11a. Differences compared to the natural sample series presented in this study most likely result from variations in initial bulk $(MgO + FeO)/SiO_2$ ratio across the whole ophicarbonate region. This also explains our low metamorphic olivine modes in Atg-ophicarbonate samples (Table 1), which we interpret to primarily represent regional metamorphic growth after brucite dehydration, when compared to the high Ol mode in the model (Fig. 11a). The presence of CaO in the ophicarbonate system stabilises the Ca-silicates tremolite and diopside. Consequently the amount of silica in the remaining phases is reduced until talc is no longer formed upon antigorite dehydration. Therefore, talc-out reaction may no longer take place at common ophicarbonate bulk compositions. The dehydration reactions antigorite-out, tremolite-out, and chlorite-out are shifted to lower temperatures compared to carbonate-free hydrous peridotite systems (Fig. B-1) by about 20 °C, 130 °C and 60 °C at 0.35 GPa, respectively. For further discussion in relation to our field observations (Section 6), the model system with 20 wt% carbonate (calcite) and 80 wt% bulk silicate serves for reference. The relevant continuous dehydration reactions with increasing temperature (Figs. 10 and 11) are:

Antigorite-out, producing Tr-ophicarbonate:

$$Atg + Cal \rightarrow Tr + Ol + Chl + fluid \quad (1)$$

Tremolite-out, producing Di-ophicarbonate:

$$Tr + Cal \rightarrow Di + Ol + fluid \quad (2)$$

Chlorite-out, producing Spl-ophicarbonate:

$$Chl + Cal \rightarrow Spl + Ol + Di + fluid \quad (3)$$

Fig. 11b portrays the prograde equilibrium fluid $X_{CO2}$ evolution as obtained from Fig. 11a in a T-$X_{CO2}$ diagram for our model system. In the closed system reaction (1) consumes antigorite along with calcite (until antigorite exhaustion) to form tremolite plus olivine plus chlorite and releases a first major pulse of $H_2O$-$CO_2$ fluid with $X_{CO2}$ of ≤0.09. Reaction (2) consumes tremolite entirely along with calcite, producing diopside plus olivine and liberating a second major pulse of $H_2O$-$CO_2$ fluid with $X_{CO2}$ of ≤0.16. Reaction (3) consumes chlorite completely, liberating a fluid with $X_{CO2}$ of ~0.16.

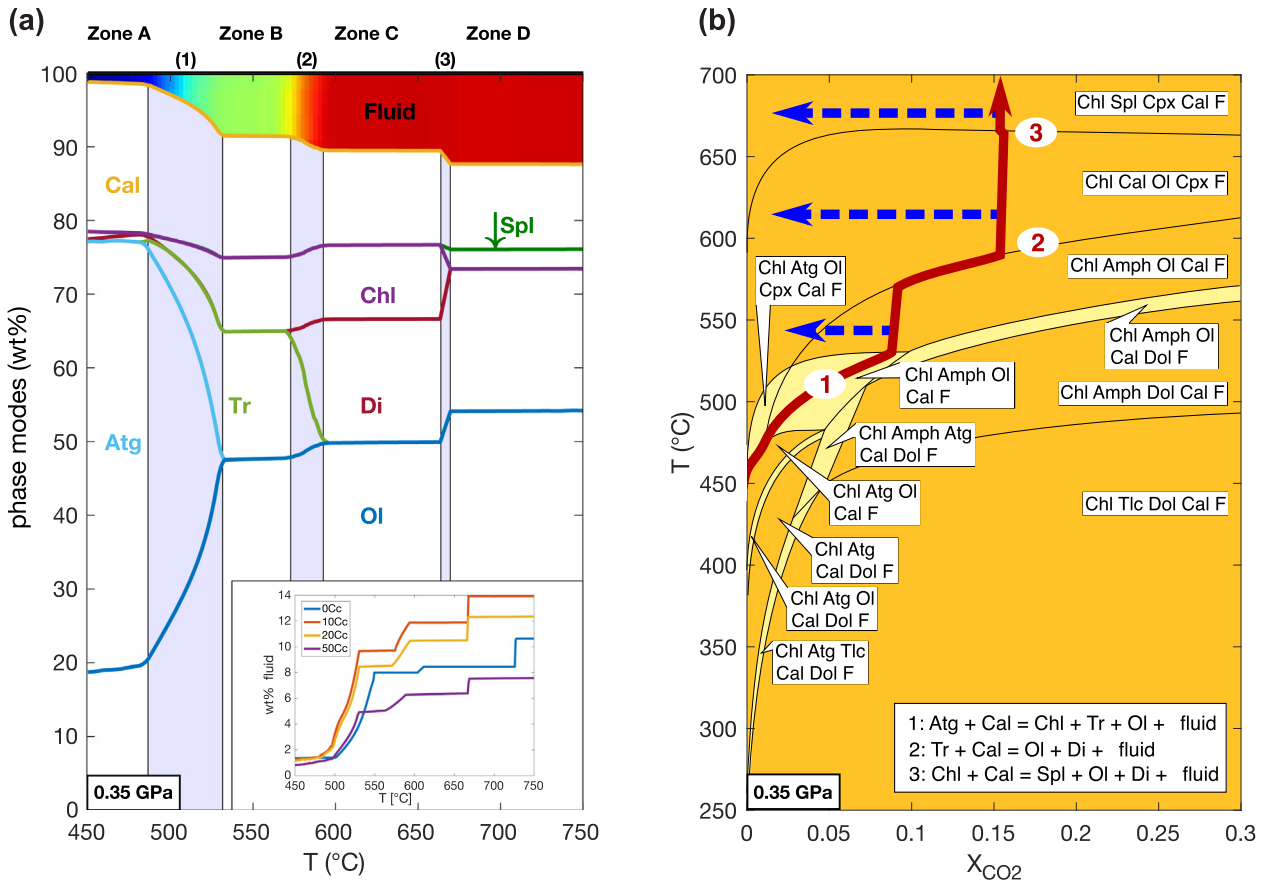


Fig. 11. (a) Modelled isobaric (0.35 GPa) closed system equilibrium evolution of meta-ophicarbonate (20 wt% calcite + 80 wt% serpentinite) phase modes from 450 − 750 °C. Numbers in brackets refer to dehydration reactions addressed in text, separating contact metamorphic zones (A = Atg-ophicarbonate; B = Tr-ophicarbonate; C = Di-ophicarbonate; D = Spl-ophicarbonate). $X_{CO2}$ colour-coding of the $H_2O$-$CO_2$ fluid corresponds to that used in Fig. 10. Small inset in (a) displays the $H_2O$-$CO_2$ fluid fractions produced for different ophicarbonate calcite-serpentinite mixtures as defined in the legend (corresponding bulk is given in table B-1, corresponding PT- pseudosections are given in figures B-1 to B-4). (b) T - $X_{CO2}$ diagram displaying the isobaric (0.35 GPa) meta-ophicarbonate (20 wt% calcite + 80 wt% serpentinite) closed system equilibrium reaction path in red illustrating reactions (1)–(3) as addressed in text. The blue dashed arrows visualise the drop in $X_{CO2}$ upon aqueous fluid ingress that causes more carbonate to react to bring the system back to rock-buffered $X_{CO2}$ conditions. Mineral abbreviations after Whitney and Evans (2010), and F stands for fluid. (For interpretation of the references to colour in this figure legend, the reader is referred to the web version of this article.)

The fate of carbonate is strongly dependent on bulk ophicarbonate composition, i.e., on the initial carbonate fraction, as well as on the amount and types of silicate minerals. While in to model ophicarbonate (20 wt% $CaCO_3$) carbonate remains stable up to to temperatures above reaction (3), in a system with less than 10 wt% bulk carbonate, the carbonate fraction can be exhausted during dehydration reactions (1), (2) or (3). The inset in Fig. 11a illustrates the variable $H_2O$-$CO_2$ fluid modes released upon progressive heating from ophicarbonate with variable carbonate fractions; however, the main devolatilisation reactions remain identical.

Employing a less hydrated but otherwise identical ophicarbonate bulk composition (20 wt% calcite:80 wt% partially serpentinised peridotite with a bulk rock $H_2O = 4.8$ wt%) produces a fluid with $X_{CO2}$ of up to 0.30 at tremolite dehydration (reaction (2)), while the $X_{CO2}$ for the chlorite dehydration fluid (reaction (3)) decreases slightly again (Fig. B-5). This example illustrates that the $X_{CO2}$ of the liberated fluid prominently depends on the bulk composition.

The relative order of reactions (2) and (3) also depends on bulk rock composition and the constraints on the solid solutions. For example, allowing for Tschermak-substitution in pyroxene and amphibole and having a bulk $Al_2O_3 \leq 1$wt% reacts chlorite out prior to tremolite.

While the modelling results above illustrate the behaviour in a closed-system, differences observed for our sample series indicate open system conditions. The ophicarbonate zone is surrounded by large masses of antigorite-serpentinite and their partial dehydration products. Because the mass of aqueous fluid liberated upon antigorite dehydration exceeds the amounts that can be stored in rock porosity at these conditions, fluids will escape and may eventually infiltrate the ophicarbonate zone where the fluids are out of equilibrium, thus triggering reactive fluid flow, the evidence for which we discuss in the following.

## 6. DISCUSSION

### 6.1. Field evidence vs. modelling: Massive $CO_2$ mobilisation

The ophicarbonate body investigated here is embedded mainly in hydrous peridotites and was formed as a coherent unit upon ocean floor serpentinisation as demonstrated by field relations including rock textures (Figs. 1 and 2) as well as bulk rock and mineral chemistry (discussed below). The comparison of mineralogical changes across the ~300 °C temperature interval documented by our field samples with those predicted by closed-system modelling reveals that the sequence of major devolatilisation reactions is identical; however, observed phase modes in samples (Table 1) differ prominently from model predictions illustrated in Fig. 11a. Tr-ophicarbonate resulting from Atg-ophicarbonate at ~480 to 530 °C preserves the original rock texture in outcrop and contains well over 50% tremolite in many cases (Fig. 1c, d). Such extreme tremolite modes combined with low carbonate modes, or absence of carbonate in several Tr-ophicarbonate samples, prominently exceed those predicted by closed system thermodynamic modelling (<20% tremolite, >10% carbonate; Fig. 11a), which therefore demonstrates open system conditions. We now base our discussion of the open-system prograde devolatilisation history of the ophicarbonate sequence upon the closed-system models, with special emphasis on the extent of decarbonation and $CO_2$ mobilisation induced by fluid ingress from dehydration of adjacent serpentinites.

Each of the three major devolatilisation reactions (1)–(3) (Fig. 11a) consumes carbonate, forming a $H_2O$-$CO_2$ fluid with $X_{CO2}$ values of between 0.09 and 0.16 (or potentially much higher, depending on ophicarbonate bulk composition; Fig. B-5), the maximum reached at reaction (2) (Figs. 10 and 11a, b, B-5). These high $X_{CO2}$ values prominently exceed those predicted to occur upon subducted slab devolatilisation of identical lithologies (e.g., Menzel et al., 2019). Consequently, the major carbonate fraction in subducting slabs can be retained beyond typical dehydration depths irrespective of whether open or closed system settings are considered (Gorman et al., 2006; Connolly, 2005; Menzel et al., 2020). In contrast, some of our rocks record >50% calcite loss at lower pressure (Fig. 1d), thus documenting massive decarbonation upon aqueous fluid infiltration, likely from adjacent dehydrating serpentinite. Because of the simple texture and composition of meta-ophicarbonate, decomposition of several tens of wt% carbonate from rock and its transformation into calcsilicate minerals can actually be recognised in the field, an observation that is so much harder to accomplish for carbonate-bearing metasediments (e.g., Ague and Nicolescu, 2014).

Upon aqueous fluid infiltration from antigorite dehydration, meta-ophicarbonate rock - fluid assemblages are out of equilibrium because resulting fluid $X_{CO2}$ values are lower than those prevailing at equilibrium conditions (examples are given by the dashed blue arrows in Fig. 11b). In order to increase fluid $X_{CO2}$ back towards the rock-buffered values, the major equilibrium dehydration reactions (1) and (2) shift to the right, thus consuming more carbonate and producing more tremolite or diopside (compare Table 1). The reaction will proceed as long as aqueous fluid is infiltrated until one of the reactants is consumed completely. If silicates (i.e. antigorite or tremolite, for reactions (1) or (2)) are the limiting reactants, further buffering of $X_{CO2}$ via carbonate mineral (Cb) consumption can be written as a general, simplified reaction like

$$\text{Low-}X_{CO2}\ \text{fluid} + \text{Cb} + \text{SiO}_2 + \text{MgO} \rightarrow \mathit{High} - X_{CO2}\mathit{fluid} + \mathit{Ca} - \mathit{silicate} \pm \mathit{Ol} \quad (4)$$

The source(s) of MgO and $SiO_2$ in this reaction can be any Ca-free (Mg,Fe)-silicate. For example, $SiO_2$ and MgO could be made available via concurrent $Al_2O_3$ increase in chlorite, and the Si/Mg ratio is balanced by the formation of additional olivine. An alternative could be the consumption of talc formed in associated talc-olivine ± chlorite rocks representing the reaction product of Atg-serpentinite dehydration at some 20 °C higher temperatures than for reaction (1) in meta-ophicarbonate (compare Fig. 10 with Fig. B-1). Because also talc has a lower Si/Mg ratio than the product Ca-silicates tremolite and diopside, excess MgO could be fixed in new olivine or possibly chlorite (recall, however, that chlorite modes are limited by $Al_2O_3$ availability), additional $SiO_2$ may be advected, or excess MgO might leave the system. Once the carbonate is consumed completely, the fluid $X_{CO2}$ will become rock-buffered by the carbonate-free assemblage to aqueous fluid ($X_{CO2} = 0$), and fluid-mediated C mobility will be minimal, corresponding to the little C that can be dissolved in water at these low-P conditions (e.g., Kelemen and Manning, 2015; Menzel et al., 2020).

The same principles operate at higher temperatures where Di-ophicarbonate is stable. We note that $X_{CO2}$ of the fluid in equilibrium with Tr-ophicarbonate is lower ($X_{CO2} \sim 0.09$) than that coexisting with Di-ophicarbonate ($X_{CO2} \sim 0.16$; Fig. 11b) for the modelled 20 wt% carbonate + 80 wt% silicate bulk composition (Table B-1). Fluid in equilibrium with Tr-ophicarbonate infiltrating Di-ophicarbonate will therefore dissolve more carbonate along with Mg-silicate like talc from talc-olivine ± chlorite rocks in clast centres or from adjacent units on its way to achieve rock-buffered, higher $X_{CO2}$ fluid conditions. Note that talc-olivine ± chlorite rocks are stable at temperatures where Tr-ophicarbonate transforms into Di-ophicarbonate (compare Fig. 10 with Fig. B-1). To the contrast, in a scenario where fluid produced by reaction (2) infiltrates spinel-olivine-diopside-calcite rocks (i.e., reaction (3) product rocks) closer to the contact, its $X_{CO2}$ may be significantly higher than the rock-buffered one at this mineral assemblage; hence, carbonate precipitation could be induced. Such a process may be relevant for the formation of metasomatic carbonates that we did not observe in the field, however, in analogy to those reported from subduction zone environments (e.g., Piccoli et al., 2016; Scambelluri et al., 2016).

At larger scale we observe that the meta-ophicarbonate zone is embedded in the Val Malenco hydrous peridotite

body that partially dehydrated in response to contact metamorphism (e.g.,Trommsdorff and Evans, 1972; Trommsdorff and Connolly, 1996). Complete dehydration of former serpentinite can produce >25 vol% aqueous fluid at lithostatic pressure (based on our model calculations; fluid volume again being bulk composition dependent as shown in Fig. 11a, inset); hence, vast amounts of moderate density aqueous fluid migrates preferably along rock discontinuities through adjacent rocks. In detail, fluid flow mechanisms are complex and beyond the scope of this paper (the reader is referred to Connolly (2010) for a summary on fluid flow regimes in metamorphic rocks). Inevitable is that the large masses of dehydration fluid escapes the site of fluid production and can have lateral and vertical upward propagation components; hence, fluids produced upon Atg-serpentinite dehydration will eventually infiltrate the ophicarbonate horizon, and this lithological discontinuity may even be favourable for channelizing fluid flow. Recent models have predicted that up-temperature fluid flow may occur around synmetamorphic plutons (Lyubetskaya and Ague, 2009) or when fluid transport occurs as porosity waves (Connolly, 2010). Irrespective of the details on the potentially complex fluid migration mechanisms and pathways, our main conclusion remains that the high modes of tremolite we observed can only be produced in an open system scenario via dissolving large masses of carbonate, thereby liberating vast amounts of $CO_2$ into mixed $H_2O$-$CO_2$ fluids escaping the contact aureole.

### 6.2. Ophicarbonate geochemistry

Meta-ophicarbonate bulk rock and mineral chemistry provides evidence for both ophicarbonate formation on the ocean floor and element (re)distribution upon prograde devolatilisation reactions. We now elaborate upon the characteristics of the original mantle rocks and the geochemical imprint resulting from ophicarbonate rock formation upon exposure on the ocean floor. We then address the compositions (modelled versus measured) of silicate minerals across the carbonate-consuming reactions. Finally, we attempt a first-order conclusion on fluid-mediated chemical modification of meta-ophicarbonate chemistry upon open system prograde metamorphism.

#### *6.2.1. Precursor peridotites*

Precursor peridotites were variably melt-depleted as revealed by fluid-immobile Th and Ta bulk rock meta-ophicarbonate values mostly <0.1 times PM concentrations, as has also been reported for ocean floor ophicarbonate from the Internal Ligurides (Cannaò et al., 2020). Besides the positive La anomaly and elevated REE concentrations relative to ocean floor ophicarbonate, chondrite-normalised REE patterns (Fig. 5b) are characteristic of melt depleted peridotites with modest influence of magmatic refertilization that is variably pronounced in Alpine orogenic peridotites and serpentinites (e.g., Müntener et al., 2010; Deschamps et al., 2013). Common indices of peridotite melt depletion (e.g., slight increases in Mg# along with a trend of increasing $MgO/SiO_2$ with decreasing $Al_2O_3/SiO_2$) cannot be employed for meta-ophicarbonate, because the ranges in ocean floor and metamorphic bulk rock major element abundance ratios (not involving CaO) prominently exceed those characteristic for variably melt-depleted peridotites (Figs. 3 and 4). Rare relic clinopyroxene in one sample of Atg-ophicarbonate and Di-ophicarbonate, respectively, possesses a hump-shaped REE pattern (Fig. 8d) that is characteristic of mantle clinopyroxene from melt-depleted peridotite, and the extent of melt depletion is less than that seen for relic clinopyroxene for example from Erro Tobbio Atg-serpentinites (Peters et al., 2020). The lowest REE concentrations are seen for the LREE, which reveals that these two samples did not undergo significant magmatic refertilization (compare Niu, 2004; Müntener et al., 2004, 2010).

#### *6.2.2. Oceanic peridotite hydration and carbonation*

Meta-ophicarbonate bulk rock compositions (Table A-1) readily identify an oceanic ophicarbonate precursor. In a ternary plot of CaO – MgO – $SiO_2$ (Fig. 3), all our Atg-ophicarbonate samples lie in the binary calcite - oceanic serpentinite mixing array, and their Mg# plot in the range so far reported for oceanic and high-P ophicarbonates (Fig. 4). The REE signatures of calcite match that of calcite precipitated from Jurassic seawater and of modern 1900 m deep Eastern North Atlantic seawater, except for the variably positive Eu anomaly of our samples (Fig. 7d). Important here is the match in the variably pronounced positive La anomalies along with variably negative Ce anomalies. Together with the typical rock textures (Fig. 1c, d) and C isotope signatures that are consistent with those of marine carbonates (Pozzorini and Früh-Green, 1996), this combined data set implies that the precursor ophicarbonate was formed on the ocean floor and does not represent some sort of metasomatic material formed upon (shallow) prograde metamorphism during collision of the Adriatic with the European plate. In fact, the peculiar LREE pattern of carbonate (Fig. 7d) dominates bulk rock meta-ophicarbonate signatures (Fig. 5b) that are therefore different from oceanic serpentinite REE patterns (e.g., Kodolányi et al., 2012; Deschamps et al., 2013).

Bulk meta-ophicarbonate rocks are variably and strongly enriched in B, U, As, Sb, W, Bi, Cd, and Sr (Fig. 5), and their patterns largely match those reported for ocean floor ophicarbonate from the Internal Ligurides (Cannaò et al., 2020). Therefore, these FME enrichments readily identify prominent mantle rock hydration and carbonation on the ocean floor (compare e.g., Kodolányi et al., 2012; Peters et al., 2017, and references therein). Atg-ophicarbonate samples thereby most closely approach seafloor hydration-carbonation-related FME enrichments since this rock preserves the trace element inventory prior to the three relevant devolatilisation reactions (Figs. 10 and 11). Atg-ophicarbonate samples MAL_1505 and MAL_1528 show moderate large ion lithophile element enrichments but display the most prominent enrichments in As and Sb, tracers that were claimed to readily identify involvement of sediment-equilibrated fluids upon serpentinisation (e.g., Hattori and Guillot, 2003; Deschamps et al., 2011; Scambelluri et al., 2019). However, because enrichments of Cs, Rb, and Ba are very modest, all our Atg-

ophicarbonate samples plot near the field characteristic for mid ocean ridge and passive margin serpentinite in a plot of Rb/U vs. Cs/U (Fig. 6), thus indicating insignificant contribution of sediment-equilibrated fluids upon ocean floor serpentinisation and carbonation. We therefore interpret the high As and Sb concentrations of some of our samples to be indicative of low-temperature hydrothermal overprint on the seafloor (compare Andreani et al., 2014) as can be relevant in an OCT setting, rather than tracing sediment-equilibrated fluid input during serpentinisation. Val Malenco Atg-ophicarbonate compositions thus suggest that chemical characteristics produced upon oceanic serpentinisation in a rifted passive margin settings (see Trommsdorff et al., 2005, for an excellent illustration) compare well to those of abyssal ophicarbonate (Cannaò et al., 2020). Both these sample series possess trace element signatures that are very similar to those of mid ocean ridge and passive margin serpentinites worldwide (e.g., Kodolányi et al., 2012; Deschamps et al., 2013; Peters et al., 2017), which in turn suggests that these geochemical signatures are also characteristic of serpentinites originating from an ocean continent transition setting, exemplified here by the hyper-extended rifted Tethyan margin of Adria (e.g., Manatschal and Müntener, 2009; Müntener et al., 2010).

#### 6.2.3. Chemical modification of meta-ophicarbonate rocks during devolatilisation and open system conditions

The massive $CO_2$-$H_2O$ fluid release associated with open system conditions will induce chemical modifications to the partially devolatilised ophicarbonate. Constraining these reliably would require knowledge of $CO_2$-$H_2O$ fluid - mineral element distribution coefficients for the ophicarbonate system at prevailing P and T, and such data are not available to our knowledge. We further recall that the initial compositional variability is large, notably for the major element inventory (Figs. 3 and 4), thus impeding a direct comparison between reactant and product bulk rock and mineral signatures. Nevertheless, we now attempt to deduce some first order constraints from our data set in combination with literature data.

The ternary plot of CaO – MgO – $SiO_2$ (Fig. 3) reveals that the Tr-ophicarbonate samples lie on the join between abyssal serpentinites and measured tremolite mineral composition, notably displaced away from the CaO corner for a rock that contained some 30–50% carbonate based on texture (Fig. 1d). We note that the LOI of Tr-ophicarbonate samples is of the order of 4 wt% when compared to the LOI of 20–32 wt% measured for Atg-ophicarbonate, thus demonstrating massive loss of mineral-bound $CO_2$ along with some $H_2O$. The Tr-ophicarbonate data are also shifted towards lower $MgO/SiO_2$ ratios from the binary calcite - serpentinite mixing field. This can be the result of fluid-mediated MgO removal or $SiO_2$ advection. Measured fluid compositional data in the systems MgO – $SiO_2$ – $H_2O$ and graphite-saturated MgO – $SiO_2$ – COH (800 °C/1 GPa) are plotted in Fig. 3 for reference (Tumiati et al., 2017). It can be seen that the $SiO_2/MgO$ ratio prominently increases for COH-fluids (along with a ~5-fold concentration increase; Tumiati et al., 2017) when compared to C-free aqueous fluid. This thus suggests that the shift away from the binary calcite - serpentinite mixing field observed for the Tr-ophicarbonate samples represents a prominent fluid-induced signal of $SiO_2$ addition in an open system. The position of the Di-ophicarbonate samples just at the $SiO_2$-rich edge of the calcite - serpentinite mixing field in this ternary plot is also consistent with such an interpretation.

An interesting question is whether, and if so how, fluid metasomatism upon devolatilisation would affect Mg# of bulk rock and silicate compositions. For bulk rocks we note that Tr-ophicarbonate samples show higher while Di-ophicarbonate samples show lower Mg# when compared to the range measured for Atg-ophicarbonate samples in this work, and our data fall within the large range reported for ocean floor and high-P ophicarbonates (Fig. 4). Consequently, our data do not offer further constraints as to how Mg# in ophicarbonate bulk rock compositions may evolve with progressive devolatilisation. In a next step we compare modelled (closed-system) mineral compositional data for MgO, FeO, CaO, $SiO_2$, and $Al_2O_3$ with measured average compositions for the minerals participating in reactions (1), (2), and (3) (Table A-8). We take average measured mineral compositions in order to attenuate bulk composition variabilities between individual samples. We note here that calculated antigorite compositions in Atg-ophicarbonate deviate significantly from observations due to the modelled G-x relations that resulted in unrealistic compositions (electronic supplementary material). For Tr-ophicarbonate, silicate mineral data are complete, and the model predicts silicate coexistence with residual calcite whereas we observe new dolomite (MAL_1602). The product mineral assemblage of reaction (1), tremolite + olivine + chlorite, displays very good agreement between measured and modelled compositions (including Mg#), thus further supporting our interpretation that these calcite-free rocks in Zone B originate from Atg-ophicarbonate and that equilibrium conditions largely prevailed through $X_{CO2}$ buffering. That modelled and measured Mg# agree well also suggests that Mg is not strongly fractionated from Fe via fluid-mediated processes, which we interpret to indicate that loss of Mg and Fe from the rock upon Tr-ophicarbonate formation at ~500 °C/0.35 GPa is subordinate at best. The modelled reaction (2) product mineral assemblage diopside + olivine with stable chlorite is in agreement with our Di-ophicarbonate samples. The modelled average diopside Mg# is higher while the modelled average olivine Mg# is lower than the measured compositions; however, measured and modelled ranges largely overlap, thus suggesting that differences and variations in bulk compositions may be relevant for our Di-ophicarbonate samples. Chlorite compositions also display similar ranges for modelled and measured compositions, whereby modelled ones tend to be more magnesian. Regarding the calcite compositions for Zone C we note the very low $FeO_{tot}$ contents for our measured data that are not predicted by the model results, possibly again hinting towards variations in bulk rock compositions.

Compositional evidence of precursor calcite for Ca-silicates can be recognised in reaction product tremolite and diopside of Tr-ophicarbonate and Di-ophicarbonate.

For example, their REE concentrations are prominently higher when compared to metamorphic tremolite and diopside from regional metamorphic Atg-ophicarbonate (Fig. 8b, d) and to tremolite from Atg-serpentinites (Zihlmann, 2012; however, intra-sample variations are significant). This REE enrichment goes along with a distinct enrichment in Sr, thus confirming that a "carbonate trace element signal" is present in the prograde silicate minerals, notably in diopside. Together, this suggests redistribution of carbonate REE and Sr into high-T tremolite, a product of the reaction of antigorite with calcite, and into diopside forming after tremolite plus calcite in mineral zone C. Conspicuous is the fact that neither tremolite nor diopside (except for Tr-ophicarbonate sample MAL_1612) display the positive La anomaly characteristic for seafloor calcite or bulk Atg-ophicarbonate. We interpret this to indicate that notably for Tr-ophicarbonate, Atg-serpentintite derived fluid ingress diluted the carbonate REE signal to beyond recognition, in both bulk rock and tremolite and chlorite mineral data. Even metamorphic dolomite, formed according to a reaction like Atg + Cal → Tr + Ol + Chl + Dol + fluid in Tr-ophicarbonate (sample MAL_1602), does not possess this positive La anomaly (Fig. 7d). This further corroborates that Tr-ophicarbonate samples represent the most fluid-modified compositions represented by our data set.

Having argued for prominent open system fluid metasomatism, we can now test whether the FME typically employed to assess fluid-mediated chemical processes in subducting serpentinites also display evidence for such processes in meta-ophicarbonate types. A first observation is that carbonates do not seem to represent a relevant host for most FME except for Sr and ±B (Fig. 7c, d), hence, carbonates in ophicarbonate have a subordinate effect on bulk rock FME systematics. Therefore, we can compare our sample FME systematics to those established for ocean floor serpentinites and subducted equivalents (e.g., Deschamps et al., 2013, Peters et al., 2017; Scambelluri et al., 2019). A first order observation is the fact that the antigorite, chlorite and regional metamorphic tremolite and diopside in our samples possess PM-normalised FME patterns that largely reflect bulk ophicarbonate patterns (Figs. 5–9). In detail, Tr-ophicarbonate bulk rock data display among the lowest enrichments in As and Sb and the lowest Sr enrichment of the entire rock suite (Fig. 5), thus suggesting that significant fractions of As, Sb, and Sr were lost to the escaping fluid. To the contrast, concentrations of the FME Rb, Ba, W, Bi, Pb, and In are within the range observed for the entire sample suite, and B and Cs are even higher. Elevated B concentrations could result from input via Atg-serpentinite derived fluids, and the high Cs concentrations could indicate interaction of these fluids with Margna gneisses along the fluid migration path. For Di-ophicarbonate we note overall higher Ni concentrations in diopside and olivine when compared to those in Tr-ophicarbonate, which may be indicative of pentlandite consumption upon tremolite dehydration.

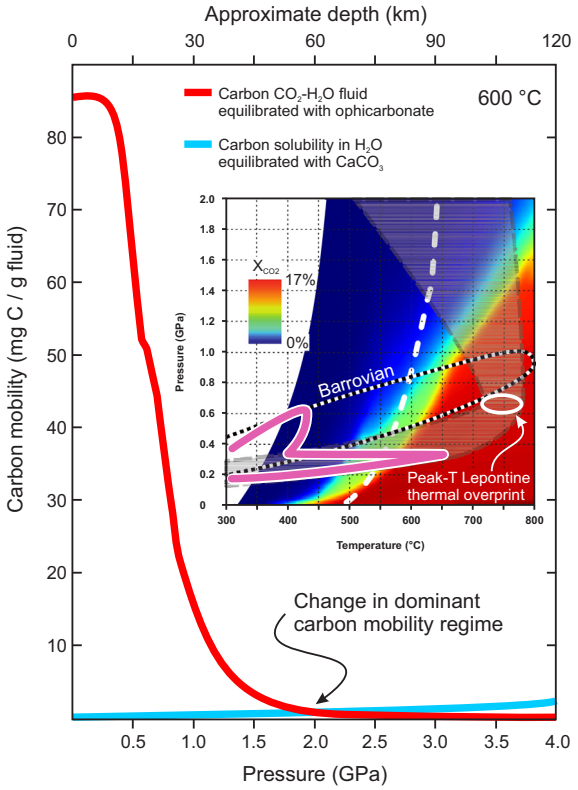


Fig. 12. Isothermal (600 °C) curves of carbon mobility as a function of increasing pressure covering 0–120 km depth for carbon solubility in $H_2O$ equilibrated with $CaCO_3$ (blue curve, after Kelemen and Manning, 2015) and for ophicarbonate rock-buffered, mixed $H_2O$-$CO_2$ fluid (red curve, this work). This figure emphasizes that $CO_2$ is mobilised most efficiently at temperatures exceeding 550 °C and pressures well below 1.5 GPa as rock-buffered, mixed $H_2O$-$CO_2$ fluids. Clearly, these numbers vary as a function of bulk composition; however, the overall implications remain. The P-T diagram inset sketches three metamorphic P-T paths enabling prominent $CO_2$ mobilisation associated with collisional orogens. (i) Contact metamorphic heating (pink curve; the Bergell case documented here). (ii) Late metamorphic heating in collisional orogens as exemplified by the Central European Alps (semi-transparent gray band). The white ellipse represents the peak-T Lepontine thermal overprint (P-T constraints from migmatisation after Burri et al., 2005), possibly following high-P peak subduction metamorphism at pressures exceeding Y-axis scale (sketched after Brouwer et al., 2005). (iii) An example of Barrovian metamorphic P-T path (black-white dashed P-T loop; Hyndman, 2019). The white dashed line displays antigorite dehydration for harzburgitic bulk composition (taken from Fig. B-1). Colour-coding represents $X_{CO2}$ values for ophicarbonate rock-buffered $H_2O$-$CO_2$ fluid (model composition 20 wt% calcite – 80 wt% serpentinite displayed in Figs. 10 and 11). Note that carbon solubility in $H_2O$ equilibrated with $CaCO_3$ (blue curve) has to be considered as minimum solubility because speciation is highly uncertain, and complex species are expected to increase carbon solubility in aqueous fluid (e.g., Tumiati et al., 2017). (For interpretation of the references to colour in this figure legend, the reader is referred to the web version of this article.)

### 6.3. Relevance for the global carbon cycle

Our study represents an exceptionally well controlled field example for massive carbonate decomposition triggered by contact metamorphic dehydration reactions, which we take as a proxy for processes operating at large-scale $CO_2$ mobilisation from high heat flow settings. We now put this finding into an orogen-scale perspective. Fig. 12 demonstrates that bulk fluid carbon mobility in mixed $H_2O$-$CO_2$ fluids at hot, low-P conditions exceeds that of carbon solubility in $H_2O$ equilibrated with $CaCO_3$ (Kelemen and Manning, 2015) by much over an order of magnitude. Radically more carbon can be mobilised in mixed $H_2O$-$CO_2$ fluids at these conditions. For the 600 °C isotherm, the change in dominant carbon mobility regime (mixed $H_2O$-$CO_2$ fluid versus C dissolved in aqueous fluid) occurs somewhere between 40 and 60 km depth (Fig. 12; depending on bulk composition). Consequently, hot, low to moderate pressure, fluid-saturated conditions are most relevant for mobilising carbon fixed in rocks, while subduction metamorphism offers comparatively modest $CO_2$ mobilisation potential. This is because typical subduction geotherms even for hot slab surfaces (compare Syracuse et al., 2010) do not intersect high $X_{CO2}$ fluid conditions on their prograde path.

As a consequence, other geological settings may be equally relevant for prominent $CO_2$ mobilisation. Fig. 12 inset depicts the P-T-t paths of contact metamorphic aureoles around shallow intrusions in exhuming orogens (the case study here) and of heating post-dating a possible high-P metamorphic episode (e.g., Brouwer et al., 2005) as is also realised in the Central European Alps. This heating event is referred to as the Lepontine thermal overprint, reaching T-P conditions of about 750 °C/0.65 GPa in the Southern Steep Belt (Burri et al., 2005). Additionally, Fig. 12 inset also displays a typical Barrovian metamorphic T-P loop reaching peak conditions of 800 °C/1 GPa (compare e.g., Hyndman, 2019). While the three metamorphic scenarios are prominently different regarding their geotectonic setting, they all can reach high temperatures along with moderate to low pressures. Setting these scenarios in relation to ophicarbonate rock-buffered fluid $X_{CO2}$ values reveals that their peak temperature conditions all intersect the domain of high $X_{CO2}$ fluids; hence, they offer great potential for massive $CO_2$ mobilisation. While $X_{CO2}$ fluid values are very sensitive to the buffering rock bulk composition, hence mineralogy (e.g., Kerrick and Connolly, 1998; Gorman et al., 2006; Menzel et al. 2019; this work), the first-order systematics remain comparable between metaophicarbonate and carbonaceous metasediments as long as excess aqueous fluid is present (compare Ague and Nicolescu, 2014). As an important consequence, our findings are relevant to carbonated silicate rocks of orogenic belts, from which prominent masses of carbonate-bound $CO_2$ can thus be liberated upon high-temperature and moderate to low pressure regional metamorphism, provided that large amounts of $H_2O$ are available.

#### 6.3.1. Volcanic outgassing

Volcanic emissions to the atmosphere along convergent plate boundaries are characterised by C and H isotopes indicative of significant assimilation of crustal carbonate that may dominate global volcanic $CO_2$ fluxes atop subduction zones as opposed to slab carbon, notably for continental arcs (Mason et al., 2017). For example, He and C isotopic signatures of fumaroles at Popocatepetl, one of the most prominent present-day $CO_2$ emitter volcanoes on Earth, indicate a significant contribution of marine carbonate (Goff et al., 1998). Because solubilities of $CO_2$ in hydrated calcalkaline magmas are modest (e.g., Ghiorso and Gualda, 2015), the $CO_2$ mobilisation process in rising mixed $H_2O$-$CO_2$ fluids in response to contact metamorphism around magma reservoirs in the upper crust as identified here (Figs. 11 and 12) may be equally relevant, if not even exceeding direct magmatic $CO_2$ outgassing. Such $CO_2$ degassing may occur around active volcanoes (e.g., Kerrick and Connolly, 2001) or seep into the groundwater table where dispersion may further blur its occurrence. Collisional plate boundaries with prolific magmatism like the Eastern Pacific margin, referred to as sites of "regional contact metamorphism" by Spear (1993), might thus have had a first-order influence on past $CO_2$ emissions to the atmosphere (Kerrick and Caldeira, 1998; Ganino and Arndt, 2009; Svensen and Jamtveit, 2010).

#### 6.3.2. Diffuse outgassing along convergent plate boundaries

Our modelling demonstrates that $CO_2$ mobility is highest for metamorphic dehydration reactions at shallow upper amphibolite facies conditions (Fig. 12) as can also be achieved in high heat flow collisional orogenic settings. The typical P-T regime here evolves along clockwise P-T-t paths (with or without a high-P stage) and enables high temperatures paired with low to moderate pressures. The typical post peak pressure P-T-t paths for the Central European Alps run at high angle to fluid $X_{CO2}$ isopleths (Fig. 12 inset) notably for decompression occurring upon ongoing heating and intersect the maximum fluid $X_{CO2}$ fields at near peak temperature reached upon early exhumation. Because relevant dehydration reactions (e.g., antigorite dehydration in adjacent serpentinite, represented as white dashed line in Fig. 12), are also expected to be crossed upon heating to above ~600 °C during decompression, significant masses of rock $CO_2$ may be mobilised from former ocean floor materials at rock-buffered conditions via devolatilisation reactions or via aqueous fluid ingress. $CO_2$ degassing can thus be triggered by prograde heating arising from conductive heating triggered by slab breakoff (von Blanckenburg and Davies, 1995), slab rollback (Sizova et al., 2019), or by thermal relaxation of the crust following tectonic thickening upon continent–continent collision. These processes may operate in combination and are relevant on time scales of millions of years. Such metamorphic $CO_2$ output to the atmosphere, to our knowledge, needs to be more rigorously considered in modern models of global carbon cycling at geological time scales. Because such metamorphism occurs

at much slower rates than contact metamorphism, amagmatic $CO_2$ mobilisation along convergent plate boundaries represents a more continuous $CO_2$ supply to the atmosphere over millions of years.

For meta-ophicarbonate, three prominent stages of devolatilisation (Fig. 11a) each trigger carbon release, further sustained by the mass of aqueous fluid liberated from associated rocks like serpentinites. Meta-ophicarbonate rocks overprinted by such reactive fluid flow are composed predominantly of tremolite (diopside at higher T) and may often lack carbonate, even though initial carbonate fractions can have exceeded 50 vol%. Rocks commonly mapped as calcsilicate associated with metaperidotites in the European Alps (e.g., Pfiffner and Trommsdorff, 1998) may represent such silicate leftovers from vast carbonate mobilisation; hence, they deserve more consideration in future studies of collisional orogens in general to assess large-scale, amagmatic carbon mobilisation.

The question then arises, what happens to the large masses of $CO_2$ mobilised when $H_2O$-$CO_2$ fluids ascend through the metamorphic rock pile, i.e., what fraction of $CO_2$ may actually be outgassed to the atmosphere. In the central European Alps, the metamorphic evolution was such that deeper rock units were heating up while shallower units were already on their retrograde path, i.e., the scenario of "deep later" in Stüwe et al. (1993). Rock from shallower units are characteristically cut by omnipresent, late orogenic quartz veins formed between some 450 and 200 °C that commonly contain carbonate minerals, thus representing a $CO_2$ sink. A classical example of such hydrothermal activity are the late orogenic auriferous quartz veins in the Monte Rosa Gold District (internal NW European Alps) that formed from fluids with $X_{CO2} \sim 0.06$, which ascended over more than 10 km vertically prior to mineralisation (Pettke and Diamond, 1997) and comprise variably prominent carbonate irrespective of host rocks that are often devoid of carbonate (Diamond, 1990; Pettke et al., 2000). Widespread Alpine fissures hosting free-grown hydrothermal minerals are also variably accompanied by different carbonate types. These observations document that part of the $CO_2$ in the mixed $H_2O$-$CO_2$ fluids actually precipitated in channelized rising fluids and, more importantly, it testifies to the omnipresence of such fluids in exhuming rock units. Fluid inclusion evidence constrains the fraction of $CO_2$ in the mixed $H_2O$-$CO_2$ fluids of central Alpine fissures to commonly between 5 and 15 mol% (e.g., Mullis et al., 1994).

An important aspect to foster diffuse $CO_2$ outgassing in collisional orogens is the mode of fluid flow. Pervasive fluid flow likely prevails upon regional metamorphic $H_2O$-$CO_2$ fluid production at peak temperatures, thus maximizing fluid-rock interaction and equilibration at rock-buffered fluid $X_{CO2}$ values. To the contrast, the widespread, late metamorphic, discordant vein filling fractures addressed above document that channelized $H_2O$-$CO_2$ fluid flow predominates at least in exhuming rock units; hence, reactive fluid flow, as illustrated by omnipresent, thin alteration envelopes around such veins, and associated carbonate precipitation is minimised. Carbonate precipitation in such veins may thus be dominantly due to fluid cooling. This combined evidence documents the common occurrence in the central Alps of metamorphic mixed $H_2O$-$CO_2$ fluids with $X_{CO2}$ of the order of 0.1 that eventually seep $CO_2$ to the atmosphere, over time scales of millions of years characteristic of metamorphism in collisional orogens (compare Nesbitt et al., 1995; Becker et al., 2008; Evans et al., 2008; Groppo et al., 2017; Stewart et al., 2019).

## 7. CONCLUSIONS

Our findings demonstrate massive open-system carbonate reaction and associated $CO_2$ mobilisation triggered by metamorphic devolatilisation reactions around a shallow-to-mid-crustal contact aureole. This decarbonation process left behind calcsilicate rocks devoid of carbonate with dominant tremolite as identified in the field, or possibly diopside-rich rocks at higher temperatures. Such $CO_2$ mobilisation in hot, shallow, mixed $H_2O$-$CO_2$ fluids seems to be significantly more effective than mobilisation of C dissolved in aqueous fluids at subduction zone conditions. Orogen-scale considerations combined with evidence from the literature suggest that such contact metamorphic $CO_2$ mobilisation represents a relevant contribution to the total $CO_2$ outgassing from collisional orogenic settings.

Based on the first order resemblance of contact metamorphic heating with peak temperature conditions of clockwise P-T-t metamorphic paths characteristic for several collisional orogens and exemplified by the central European Alps, we suggest that high heat flow metamorphism may be another, much larger scale setting where prominent, amagmatic $CO_2$ mobilisation takes place. Because here time scales are millions of years, such amagmatic $CO_2$ liberation to the atmosphere represents a more continuous background supply. Together with $CO_2$ mobilisation via contact metamorphism, these combined metamorphic $CO_2$ emissions may be highly relevant in achieving steady state conditions in the global carbon cycle over millions of years.

Orogen-scale quantification of metamorphic carbon outgassing rates seems exceedingly difficult at present based on direct measurements, because the largest outgassing fraction is likely diffuse and will mix with ambient groundwater prior to reaching the atmosphere. Nevertheless, a potentially prominent contribution of such amagmatic $CO_2$ outgassing to the global carbon cycle seems to be indicated (compare also Stewart et al., 2019) and may become better testable in future, but should already nowadays be incorporated and thus explored in models of geological global carbon cycling.

## Declaration of Competing Interest

The authors declare that they have no known competing financial interests or personal relationships that could have appeared to influence the work reported in this paper.

### ACKNOWLEDGMENTS

We thank Jamie Connolly for continued support with Perple_X issues and Joerg Hermann for very fruitful discussions during

manuscript preparation. We are grateful for the very thoughtful, complementary reviews by Manuel Menzel, Chiara Groppo, and anonymous that helped to clarify and improve our contribution, and for the careful editorial handling by Ralf Halama. This work was supported in part by the Swiss National Science Foundation grant No. 200021_172688 to TP.

## APPENDIX A. SUPPLEMENTARY MATERIAL

Supplementary data to this article can be found online at https://doi.org/10.1016/j.gca.2021.02.030.

## REFERENCES

Ague J. J. and Nicolescu S. (2014) Carbon dioxide released from subduction zones by fluid-mediated reactions. *Nat. Geosci.* **7**, 355–360.

Albers E., Bach W., Klein F., Menzies C. D., Lucassen F. and Teagle D. A. H. (2019) Fluid-rock interactions in the shallow Mariana forearc: carbon cycling and redox conditions. *Solid Earth* **10**, 907–930.

Andreani M., Escartin J., Delacour A., Ildefonse B., Godard M., Dyment J., Fallick A. E. and Fouquet Y. (2014) Tectonic structure, lithology, and hydrothermal signature of the Rainbow massif (Mid-Atlantic Ridge 36°14'N). *Geochem. Geophys. Geosyst.* **15**, 3543–3571.

Becker J. A., Bickle M. J., Galy A. and Holland T. J. B. (2008) Himalayan metamorphic CO2 fluxes: Quantitative constraints from hydrothermal springs. *Earth Planet. Sci. Lett.* **265**, 616–629.

Berner R. A. (2004) *The Phanerozoic Carbon Cycle: CO2 and O2*. Oxford Univ. Press, New York.

Bretscher A. (2017) Trace element distribution and fluid chemistry during subduction related antigorite breakdown. Ph. D. Thesis, Univ. Bern.

Bretscher A., Hermann J. and Pettke T. (2018) The influence of oceanic oxidation on serpentinite dehydration during subduction. *Earth Planet. Sci. Lett.* **499**, 173–184.

Brouwer F. M., Burri T., Engi M. and Berger A. (2005) Eclogite relics in the Central Alps: PT-evolution, Lu-Hf ages and implications for formation of tectonic melange zones. *Schweiz. Mineral. Petrogr. Mitt.* **85**, 147–174.

Burri T., Berger A. and Engi M. (2005) Tertiary migmatites in the Central Alps: regional distribution, field relations, conditions of formation, and tectonic implications. *Schweiz. Mineral. Petrogr. Mitt.* **85**, 215–232.

Campbell K. A., Farmer J. D. and Des M. D. (2002) Ancient hydrocarbon seeps from the Mesozoic convergent margin of California: Carbonate geochemistry, fluids and palaeoenvironments. *Geofluids* **2**, 63–94.

Cannaò E., Scambelluri M., Bebout G. E., Agostini S., Pettke T., Godard M. and Crispini L. (2020) Ophicarbonate evolution from seafloor to subduction and implications for deep-Earth C cycling. *Chem. Geol.* **546** 119626.

Clément M., Padrón-Navarta J. A. and Tommasi A. (2019) Interplay between fluid extraction mechanisms and antigorite dehydration reactions (Val Malenco, Italian Alps). *J. Petrol.* **60**, 1935–1962.

Connolly J. A. D. (2005) Computation of phase equilibria by linear programming: A tool for geodynamic modeling and its application to subduction zone decarbonation. *Earth Planet. Sci. Lett.* **236**, 524–541.

Connolly J. A. D. (2010) The mechanics of metamorphic fluid expulsion. *Elements* **6**, 165–172.

Crocket K. C., Hill E., Abell R. E., Johnson C., Gary S. F., Brand T. and Hathorne E. C. (2018) Rare earth element distribution in the NE Atlantic: evidence for benthic sources, longevity of the seawater signal, and biogeochemical cycling. *Front. Mar. Sci.* **5**.

Dasgupta R. (2013) Ingassing, storage, and outgassing of terrestrial carbon through geologic time. *Rev. Mineral. Geochem.* **7**, 183–229.

Dasgupta R. and Hirschmann M. M. (2010) The deep carbon cycle and melting in Earth's interior. *Earth Planet. Sci. Lett.* **298**, 1–13.

Della Porta G., Webb G. E. and McDonald I. (2015) REE patterns of microbial carbonate and cements from Sinemurian (Lower Jurassic) siliceous sponge mounds (Djebel Bou Dahar, High Atlas, Morocco). *Chem. Geol.* **400**, 65–86.

Deschamps F., Guillot S., Godard M., Andreani M. and Hattori K. (2011) Serpentinites act as sponges for fluid mobile elements in abyssal and subduction zone environments. *Terra Nova* **23**, 171–178.

Deschamps F., Godard M., Guillot S. and Hattori K. (2013) Geochemistry of subduction zone serpentinites: a review. *Lithos* **178**, 96–127.

Diamond L. W. (1990) Fluid inclusion evidence for P-V-T-X evolution of hydrothermal solutions in late-Alpine gold-quartz veins at Brusson, northwest Italian Alps. *Am. J. Sci.* **290**, 912–958.

Evans K. A. (2011) Metamorphic carbon fluxes: how much and how fast? *Geology.* **39**, 95–96.

Evans M. J., Derry L. A. and France-Lanord C. (2008) Degassing of metamorphic carbon dioxide from the Nepal Himalaya. *Geochem. Geophys. Geosyst.* **9**, Q04021.

Ganino C. and Arndt N. T. (2009) Climate changes caused by degassing of sediments during the emplacement of large igneous provinces. *Geology* **37**, 323–326.

Ghiorso M. S. and Gualda G. A. R. (2015) An H2O-CO2 mixed fluid saturation model compatible with rhyolite-MELTS. *Contrib. Mineral. Petrol.* **169**, 53.

Goff F., Janik C. J., Delgado H., Werner C., Counce D., Stimac J. A., Siebe C., Love S. P., Williams S. N., Fischer T. and Johnson L. (1998) Geochemical surveillance of magmatic volatiles at Popocatepetl volcano, Mexico. *Geol. Soc. Am. Bull.* **110**, 695–710.

Gorman P. J., Kerrick D. M. and Connolly J. A. D. (2006) Modeling open system metamorphic decarbonation of subducting slabs. *Geochem. Geophys. Geosyst.* **7**, Q04007.

Groppo C., Rapa G., Frezzotti M. L. and Rolfo F. (2020) The fate of calcareous pelites in collisional orogens. *J. Metamorph. Geol.*. https://doi.org/10.1111/jmg.12568.

Groppo C., Rolfo F., Castelli D. and Connolly J. A. D. (2013) Metamorphic CO2 production from calc-silicate rocks via garnet-forming reactions in the CFAS–H2O-CO2 system. *Contrib. Mineral. Petrol.* **166**, 1655–1675.

Groppo C., Rolfo F., Castelli D. and Mosca P. (2017) Metamorphic CO2 production in collisional orogens: petrological constraints from phase diagram modeling of himalayan, scapolite-bearing, calc-silicate rocks in the NKC(FIMAS(T)-HC system. *J. Petrol.* **58**, 53–83.

Guillong M., Meier D. L., Allan M. M., Heinrich C. A. and Yardley B. W. D. (2008) SILLS: A MATLAB-based program for the reduction of laser ablation ICP–MS data of homogeneous materials and inclusions. In Laser ablation ICP-MS in the Earth Sciences: Current practices and outstanding issues (ed. P. Sylvester). Mineralogical Association of Canada Short Course Series 40, 328–333.

Guntli P. and Liniger M. (1989) Metamorphose in der Margna-Decke im Bereich Piz de la Margna und Piz Fedoz (Oberengadin). *Schweiz. Mineral. Petrogr. Mitt.* **69**, 289–301.

Hattori K. H. and Guillot S. (2003) Volcanic fronts form as a consequence of serpentinite dehydration in the forearc mantle wedge. *Geology* **31**, 525–528.

Holland T. J. B. and Powell R. (1991) A Compensated-Redlich-Kwong (CORK) equation for volumes and fugacities of CO2 and H2O in the range 1 bar to 50 kbar and 100–1600 °C. *Contrib. Mineral. Petrol.* **109**, 265–273.

Holland T. J. B. and Powell R. (1998) An internally consistent thermodynamic data set for phases of petrological interest. *J. Metamorph. Geol.* **16**, 309–343.

Hyndman R. D. (2019) Origin of regional Barrovian metamorphism in hot backarcs prior to orogeny deformation. *Geochem. Geophys. Geosys.* **20**, 460–469.

Kelemen P. B. and Manning C. E. (2015) Reevaluating carbon fluxes in subduction zones, what goes down, mostly comes up. *Proc. Natl. Acad. Sci. USA* **112**, E3997–E4006.

Kerrick D. M. (2001) Present and past nonanthropogenic CO2 degassing from the solid earth. *Rev. Geophys.* **39**, 565–585.

Kerrick D. M. and Caldeira K. (1998) Metamorphic CO2 degassing from orogenic belts. *Chem. Geol.* **145**, 213–232.

Kerrick D. M. and Connolly J. A. D. (1998) Subduction of ophicarbonates and recycling of CO2 and H2O. *Geology* **26**, 375–378.

Kerrick D. M. and Connolly J. A. D. (2001) Metamorphic devolatilization of subducted oceanic metabasalts: implications for seismicity, arc magmatism and volatile recycling. *Earth Planet. Sci. Lett.* **189**, 19–29.

Kodolányi J., Pettke T., Spandler C., Kamber B. S. and Gmeling K. (2012) Geochemistry of ocean floor and fore-arc serpentinites: constraints on the ultramafic input to subduction zones. *J. Petrol.* **53**, 235–270.

Lyubetskaya T. and Ague J. J. (2009) Effect of metamorphic reactions on thermal evolution in collisional orogens. *J. Metamorph. Petrol.* **27**, 579–600.

Manatschal G. and Müntener O. (2009) A type sequence across an ancient magma-poor ocean-continent transition: the example of the western Alpine Tethys ophiolites. *Tectonophysics* **473**, 4–19.

Mason E., Edmonds M. and Turchyn A. V. (2017) Remobilization of crustal carbon may dominate volcanic arc emissions. *Science* **357**, 290–294.

Menzel M. D., Garrido C. J., Sánchez-Vizcaíno V. L., Hidas K. and Marchesi C. (2019) Subduction metamorphism of serpentinite-hosted carbonates beyond antigorite-serpentinite dehydration (Nevado-Filabride Complex, Spain). *J. Metamorph. Geol.* **37**, 681–715.

Menzel M. D., Garrido C. J. and Sánchez-Vizcaíno V. L. (2020) Fluid-mediated carbon release from serpentinite-hosted carbonates during dehydration of antigorite-serpentinite in subduction zones. *Earth Planet. Sci. Lett.* **531** 115964.

Mullis J., Dubessy J., Poty B. and O'Neil J. (1994) Fluid regimes during late stages of a continental collision – physical, chemical, and stable isotope measurements of fluid inclusions in fissure quartz from a geotraverse through the Central Alps, Switzerland. *Geochim. Cosmochim. Acta* **58**, 2239–2267.

Müntener O. and Hermann J. (1996) The Val Malenco lower crust–upper mantle complex and its field relations (Italian Alps). *Schweiz. Mineral. Petrogr. Mitt.* **76**, 475–500.

Müntener O., Pettke T., Desmurs L., Meier M. and Schaltegger U. (2004) Refertilization of mantle peridotite in embryonic ocean basins: trace element and Nd isotopic evidence and implications for crust-mantle relationships. *Earth Planet. Sci. Lett.* **221**, 293–308.

Müntener O., Manatschal G., Desmurs L. and Pettke T. (2010) Plagioclase peridotites in ocean-continent transitions: refertilized mantle domains generated by melt stagnation in the shallow mantle lithosphere. *J. Petrol.* **51**, 255–294.

Nesbitt B. E., Mendoza C. A. and Kerrick D. M. (1995) Surface fluid convection during Cordilleran extension and the generation of metamorphic CO2 contributions to Cenozoic atmospheres. *Geology* **23**, 99–101.

Niu Y. L. (2004) Bulk-rock major and trace element compositions of abyssal peridotites: implications for mantle melting, melt extraction and post-melting processes beneath mid-ocean ridges. *J. Petrol.* **45**, 2423–2458.

Palme H. and O'Neill H. S. C. (2014) Cosmochemical estimates of mantle composition. In *Treatise on Geochemistry*, vol. 3 (eds. H. D. Holland and K. K. Turekian), second ed. Elsevier, pp. 1–39.

Peters D. and Pettke T. (2017) Evaluation of major to ultra trace element bulk rock chemical analysis of nanoparticulate pressed powder pellets by LA-ICP-MS. *Geostand. Geoanal. Res.* **41**, 5–28.

Peters D., Bretscher A., John T., Scambelluri M. and Pettke T. (2017) Fluid-mobile elements in serpentinites: constraints on serpentinisation environments and element cycling in subduction zones. *Chem. Geol.* **466**, 654–666.

Peters D., Pettke T., John T. and Scambelluri M. (2020) The role of brucite in water and element cycling during subduction – insights from Erro Tobio (Liguria, Italy). *Lithos* **360–361** 105431.

Pettke T. and Diamond L. W. (1997) Oligocene gold quartz veins at Brusson, NW Alps: Sr isotopes trace the source of ore-bearing fluid to over a 10 km depth. *Econ. Geol.* **92**, 389–406.

Pettke T., Diamond L. W. and Kramers J. D. (2000) Mesothermal gold lodes in the north-western Alps: a review of genetic constraints from radiogenic isotopes. *Eur. J. Mineral.* **12**, 213–230.

Pettke T., Oberli F., Audétat A., Guillong M., Simon A. C., Hanley J. J. and Klemm L. M. (2012) Recent developments in element concentration and isotope ratio analysis of individual fluid inclusions by laser ablation single and multiple collector ICP-MS. *Ore Geol. Rev.* **44**, 10–38.

Pfiffner M. and Trommsdorff V. (1998) The high-pressure ultramafic-mafic-carbonate suite of Cima Lunga-Adula, Central Alps: excursions to Cima di Gagnone and Alpe Arami. *Schweiz. Mineral. Petrogr. Mitt.* **78**, 337–354.

Piccoli F., Brovarone A. V., Beyssac O., Martinez I., Ague J. J. and Chaduteau C. (2016) Carbonation by fluid-rock interactions at high-pressure conditions: implications for carbon cycling in subduction zones. *Earth Planet. Sci. Lett.* **445**, 146–159.

Piccoli F., Hermann J., Pettke T., Connolly J. A. D., Kempf E. D. and Duarte J. F. V. (2019) Subducting serpentinites release reduced, not oxidized, aqueous fluids. *Sci. Rep.* **9**.

Pozzorini D. and Früh-Green G. L. (1996) Stable isotope systematics of the Ventina Ophicarbonate Zone, Bergell contact aureole. *Schweiz. Mineral. Petrogr. Mitt.* **76**, 549–564.

Rapa G., Groppo C., Rolfo F., Petrelli M., Mosca P. and Perugini D. (2017) Titanite-bearing calc-silicate rocks constrain timing, duration and magnitude of metamorphic CO2 degassing in the Himalayan belt. *Lithos.* **292–293**, 364–378.

Salters V. J. M. and Stracke A. (2004) Composition of the depleted mantle. *Geochem. Geophys. Geosyst.* **5**, Q05B07.

Scambelluri M., Pettke T., Rampone E., Godard M. and Reusser E. (2014) Petrology and trace element budgets of high-pressure peridotites indicate subduction dehydration of serpentinized mantle (cima di Gagnone, Central Alps, Switzerland). *J. Petrol.* **55**, 459–498.

Scambelluri M., Bebout G. E., Belmonte D., Gilio M., Campomenosi N., Collins N. and Crispini L. (2016) Carbonation of subduction-zone serpentinite (high-pressure ophicarbonate; Ligurian Western Alps) and implications for the deep carbon cycling. *Earth Planet. Sci. Lett.* **441**, 155–166.

Scambelluri M., Cannaò E. and Gilio M. (2019) The water and fluid-mobile element cycles during serpentinite subduction. A review. *Eur. J. Mineral.* **31**, 405–428.

Sieber M. J., Hermann J. and Yaxley G. M. (2018) An experimental investigation of C-O-H fluid-driven carbonation of serpentinites under forearc conditions. *Earth Planet. Sci. Lett.* **496**, 178–188.

Sizova E., Hauzenberger C., Fritz H., Faryad S. W. and Gerya T. (2019) Late orogenic heating of (ultra)high pressure rocks: Slab rollback vs. slab breakoff. *Geosciences* **9**(12), 499.

Spandler C., Martin L. H. J. and Pettke T. (2012) Carbonate assimilation during magma evolution at Nisyros (Greece), South Aegean Arc: evidence from clinopyroxenite xenoliths. *Lithos* **146**, 18–33.

Spear F. S. (1993) Metamorphic phase equilibria and pressure-temperature-time paths. Mineralogical Society of America Monograph 1.

Stewart E. M., Ague J. J., Ferry J. M., Schriffies C. M., Tao R.-B., Isson T. I. and Planavsky N. J. (2019) Carbonation and decarbonation reactions: implications for planetary habitability. *Am. Min.* **104**, 1369–1380.

Stüwe K., Will T. M. and Zhou S. H. (1993) On the timing relationship between fluid production and metamorphism in metamorphic piles - some implications for the origin of post-metamorphic gold mineralisation. *Earth Planet. Sci. Lett.* **114**, 417–430.

Svensen H. and Jamtveit B. (2010) Metamorphic fluids and global environmental changes. *Elements* **6**, 179–182.

Syracuse E. M., van Keken P. E. and Abers G. A. (2010) The global range of subduction zone thermal models. *Phys. Earth Planet. Inter.* **183**, 73–90.

Trommsdorff V., Piccardo G. B. and Montrasio A. (1993) From magmatism through metamorphism to sea floor emplacemenet of subcontinental Adria lithosphere during pre-Apline rifting (Malenco, Italy). *Schweiz. Mineral. Petrogr. Mitt.* **71**, 191–203.

Trommsdorff V. and Connolly J. (1996) The ultramafic contact aureole about the Bregaglia (Bergell) tonalite: isograds and a thermal model. *Schweiz. Mineral. Petrogr. Mitt.* **76**, 537–547.

Trommsdorff V. and Evans B. W. (1972) Progressive metamorphism of antigorite schist in the Bergell tonalite aureole (Italy). *Am. J. Sci.* **272**, 423–437.

Trommsdorff V. and Evans B. W. (1977) Antigorite-ophicarbonates: contact metamorphism in Valmalenco, Italy. *Contrib. Mineral. Petrol.* **62**, 301–312.

Trommsdorff V., Montrasio A., Hermann J., Müntener O., Spillmann P. and Gieré R. (2005) The geological map of Valmalenco. *Schweiz. Mineral. Petrogr. Mitt.* **85**, 1–13.

Tumiati S., Tiraboshi C., Sverjensky D. A., Pettke T., Recchia S., Ulmer P., Miozzi F. and Poli S. (2017) Silicate dissolutiojn boosts the CO2 concentrations in subduction fluids. *Nat. Commun.* **18**, 1–11.

Vitale-Brovarone A., Chu X., Martin L., Ague J. J., Monie P., Groppo C., Martinez I. and Chaduteau C. (2018) Intra-slab COH fluid fluxes evidenced by fluid-mediated decarbonation of lawsonite eclogite-facies altered oceanic metabasalts. *Lithos* **304**, 211–229.

Von Blanckenburg F. and Davies J. H. (1995) Slab breakoff - a model for syncollisional magmatism and tectonics in the alps. *Tectonics* **14**, 120–131.

Whitney D. L. and Evans B. W. (2010) Abbreviations for names of rock-forming minerals. *Am. Mineral.* **95**, 185–187.

Zihlmann B. (2012) The distribution of major and trace elements in the serpentinites in Valmalenco. M. Sc. thesis, Univ. Bern.

*Associate editor:* Ralf Halama